Tectonics

RESEARCH ARTICLE
10.1029/2018TC005203

Cretaceous to Middle Cenozoic Exhumation History of the Cordillera de Domeyko and Salar de Atacama Basin, Northern Chile

Susana Henriquez[1], Peter G. DeCelles[1], and Barbara Carrapa[1]

[1]Department of Geosciences, University of Arizona, Tucson, AZ, USA

Key Points:
- The Cordillera de Domeyko experienced exhumation during the upper Cretaceous, Paleocene, Eocene, and Oligocene
- The Cordillera de Domeyko experienced ~2.5-3.3 km of exhumation above major structures
- Regional unconformities in the Salar de Atacama basin correspond to periods of migration of the orogenic front at ~65 and between 40 and 50 Ma

Supporting Information:
- Supporting Information S1
- Table S1
- Table S2

Correspondence to:
S. Henriquez,
susanahg@email.arizona.edu

Citation:
Henriquez, S., DeCelles, P. G., & Carrapa, B. (2019). Cretaceous to middle Cenozoic exhumation history of the Cordillera de Domeyko and Salar de Atacama basin, northern Chile. *Tectonics*, *38*, 395–416. https://doi.org/10.1029/2018TC005203

Received 22 JUN 2018
Accepted 5 DEC 2018
Accepted article online 26 DEC 2018
Published online 1 FEB 2019

Abstract Spatiotemporal patterns of deformation and exhumation in the central Andes are key parameters for reconstructing the kinematic history of the orogenic belt. Previous studies of the retroarc thrust belt document overall eastward propagation of deformation since the late Eocene, but the amount and timing of exhumation during the early phase of Andean orogeny remains largely unconstrained, particularly in the modern forearc region. In order to determine the timing and amount of exhumation prior to the late Eocene, we employed a multidating approach combining zircon U-Pb geochronology with apatite fission track and apatite (U-Th)/He thermochronology. We focus on the low-temperature cooling history of the Cordillera de Domeyko thrust belt and synorogenic deposits in the Salar de Atacama basin. Our results show Late Cretaceous to Oligocene cooling and exhumation in the Cordillera de Domeyko. The distribution of cooling ages in the forearc indicates three periods of exhumation: ~86–65, ~65–50, and 50–28 Ma. The amount of cooling was variable in space and time but requires total exhumation of ~2.5–3.3 km of rocks above major structures in the thrust belt. Regional unconformities in the Salar de Atacama basin correlate with periods of eastward migration of the orogenic front at ~65 Ma and ~50–40 Ma. Pulses of deformation at the front of the thrust belt alternated with periods of out-of-sequence hinterland deformation and exhumation. Overall, our data show that shortening in the central Andes commenced during the Late Cretaceous (as early as ~86 Ma) and that deformation (shortening) and exhumation were coupled in space and time.

1. Introduction

The Andes are the largest topographic feature on Earth associated with an active Cordilleran-type orogenic system. In its central, widest and highest part (16–26°S), the orogen comprises a forearc, a high-elevation (~3,500 m) hinterland plateau (the Altiplano-Puna plateau), an eastward vergent thrust belt (the Eastern Cordillera and Sub-Andean zone), and an eastward migrating foreland basin (e.g., Allmendinger et al., 1997; Beck & Zandt, 2002; DeCelles et al., 2011; Horton, 2005; Horton et al., 2001; Isacks, 1988; McQuarrie, 2002; Oncken et al., 2006).

The timing of onset of Andean mountain building remains a topic of active research. Estimates range between the Late Cretaceous for its western part (Arriagada et al., 2006; Mpodozis et al., 2005) and Paleocene-Eocene for the eastern retroarc region (e.g., Carrapa & DeCelles, 2015; DeCelles et al., 2015; Eichelberger et al., 2015; Oncken et al., 2006; Quade et al., 2015). Evidence from the retroarc region includes the development of a regional foreland basin, which requires the existence of a contemporaneous thrust belt (DeCelles et al., 2011; DeCelles & Horton, 2003; Horton, 2005), and stable isotope paleoaltimetry data sets that indicate high regional elevations during Eocene time (Canavan et al., 2014; Quade et al., 2015). In the western part of the central Andes, onset of orogeny is suggested by upper Cretaceous (~79 Ma) growth strata in the Cordillera de Domeyko (Arriagada et al., 2006; Bascuñán et al., 2015). However, the timing of significant regional shortening and crustal thickening in the western part of the central Andes, and its relation to deformation and basin development farther east in the retroarc region, remain sparsely documented.

In this paper we present new low-temperature thermochronological data to address the problem of orogenic timing in the western central Andes. The utility of thermochronological data in determining the timing of orogeny is based on the assumption that erosion of topographic relief generated by thrust faulting is the main mechanism for exhuming rocks in a fold-thrust belt (e.g., Ehlers & Farley, 2003; McQuarrie & Ehlers, 2017). Particularly useful are low-temperature thermochronometers such as apatite (U-Th)/He (AHe) and apatite

fission track (AFT) methods, which allow quantification of the cooling history and inferred exhumation of the upper ~4–1 km of crust (e.g., Reiners & Brandon, 2006).

Although thermochronological studies have constrained exhumation along the axis of the Cordillera de Domeyko and the Coastal Cordillera (e.g., Juez-Larré et al., 2010; Maksaev & Zentilli, 1999), very little information is available from the eastern side of the Cordillera de Domeyko and in the adjacent upper Cretaceous to Oligocene foreland basin deposits. In an effort to test the hypothesis that the western central Andes experienced growth since the Late Cretaceous (Arriagada et al., 2006; Mpodozis et al., 2005), we quantify the amount and distribution of exhumation due to shortening in the early orogenic wedge by documenting the cooling history of upper Cretaceous to Eocene rocks in the retroarc region of northern Chile (between 22° and 24°S). We present new zircon U-Pb and AFT and AHe data from bedrock and granitic clasts from the Cordillera de Domeyko and Salar de Atacama basin. We combine our results with existing data to show that the Salar de Atacama basin records exhumation of the Cordillera de Domeyko as early as ~86 Ma. Furthermore, we demonstrate that although exhumation was nonuniform, it has migrated mostly eastward due to the propagation of the thrust belt, widening and thickening the orogen at least since 65 Ma.

2. Tectonic Setting

2.1. Forearc Geology

The modern forearc region of the central Andes, between latitudes 22° and 24 °S, can be divided into four morphotectonic zones oriented subparallel to the trench. From west to east these include the Coastal Cordillera, Central Depression, Cordillera de Domeyko, and Salar de Atacama basin (Figure 1).

The Coastal Cordillera is a mountain range with 1–2 km of elevation extending along the coast of northern Chile. It is composed of lower Jurassic to lower Cretaceous volcano-sedimentary and intrusive rocks (Garcia, 1967) related to the initiation of subduction along the western edge of South America (e.g., Charrier et al., 2007). The Central Depression is occupied by an Eocene to Pliocene sedimentary basin located at an elevation of ~1 km (Hartley et al., 2000; Hartley & Evenstar, 2010; Sáez et al., 1999). Differential uplift of the Coastal Cordillera with respect to the Central Depression from Oligocene to present (Hartley et al., 2000) was related to normal and strike-slip movements along the Atacama Fault Zone (Figure 1; e.g., Okada, 1971; González et al., 2003).

Rising to an average elevation of ~3 km, the Cordillera de Domeyko (CD) lies east of the Central Depression and exposes rocks ranging in age from Neoproterozoic to Miocene. During the Jurassic to early Cretaceous, the CD hosted two back-arc basins: the marine Domeyko-Tarapaca basin and an unnamed volcano-sedimentary basin (e.g., Garcia, 1967; Marinovic & García, 1999). By the Late Cretaceous, the volcanic arc had migrated into the CD (~86–66 Ma, Quebrada Mala Formation; Marinovic & García, 1999; Basso & Mpodozis, 2012). Between the Paleocene and Eocene, the magmatic arc migrated from the axis of the CD (61–53 Ma, Cinchado Formation; Marinovic & García, 1999) to its eastern side (~47–37 Ma, e.g., Campbell et al., 2006; Figure 1). The last period of magmatic activity was coeval with early stages of sedimentation in an extensional to transtensional sedimentary basin in the CD (<52–47 Ma to upper Pliocene, Calama Basin; May et al., 1999, 2005; Pananont et al., 2004).

Directly east of the CD is the Salar de Atacama (SA) basin, which is filled with a thick succession of Cretaceous-Cenozoic sedimentary rocks that partly records the erosion of the western part of the central Andes (e.g., Jordan et al., 2007; Mpodozis et al., 2005). The basin corresponds to a negative topographic anomaly on top of a strong positive isostatic residual anomaly (Reutter et al., 2006) related to the *Central Andean Gravity High* (Götze & Krause, 2002). Several interpretations have been proposed for the origin of SA basin, including an extensional back-arc basin (Charrier & Reutter, 1994; Flint et al., 1993), inversion of an extensional basin (Muñoz et al., 2002; Macellari et al., 1991), and a flexural foreland basin (Arriagada et al., 2006; Jordan et al., 2007; Muñoz et al., 1997). The most recent work favors a foreland basin between Late Cretaceous and early Oligocene time (Arriagada et al., 2006; Bascuñan et al., 2015; Jordan et al., 2007; Mpodozis et al., 2005). The SA basin contains about 4 km of mostly alluvial sedimentary rocks exposed along the El Bordo Escarpment (Figure 2). The modern eastern margin of the SA basin is a west dipping slope where Cenozoic strata in the basin onlap a west dipping unconformity (Jordan et al., 2007). There, a west vergent monocline uplifted relief to the east 2,320 m (±1,050 m) since ~10 Ma (Jordan et al., 2010).

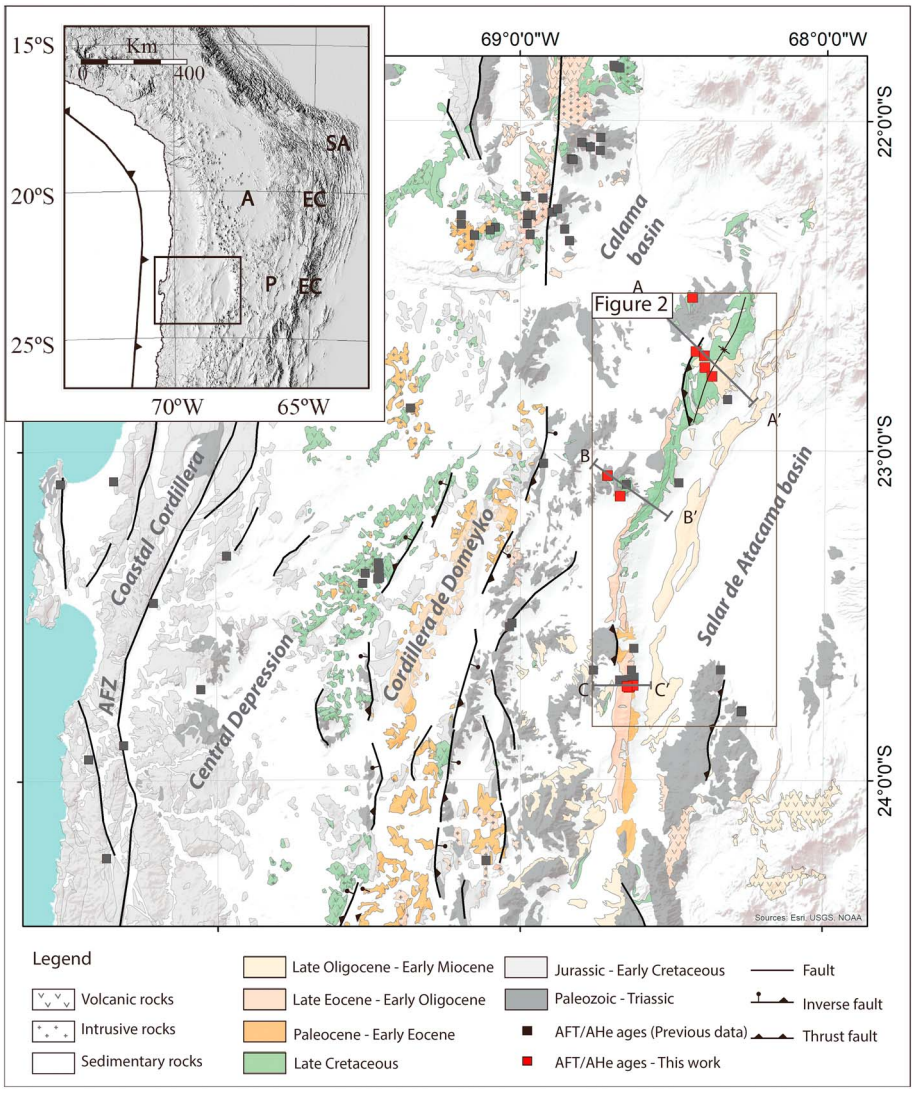

Figure 1. Geologic map of the forearc (modified from Servicio Nacional de Geología y Minería (2003)) showing the distribution of upper Cretaceous to early Miocene rocks, main structures, and the location of previous and new thermochronological data. Inset: A = Altiplano plateau; P = Puna Plateau; EC = Eastern Cordillera; SA = Subandean ranges. AFT = apatite fission track.

2.1.1. Structure of the Cordillera de Domeyko and El Bordo Escarpment

Structurally, the CD is dominated by elongated north-south trending basement ridges uplifted by north-south striking, high-angle reverse faults. Structural vergence varies along strike such that thick-skinned *pop-up* structures propagated shortening into the Mesozoic and Cenozoic sedimentary cover (Amilibia et al., 2008). The north-south striking thrusts are thought to be controlled by inversion, as early as ~90 Ma, of preexisting normal faults associated with the Mesozoic Domeyko-Tarapaca basin (Amilibia et al., 2008). To the east, a thin-skinned, east verging fold-thrust belt propagated into the Cenozoic sedimentary fill of the SA basin (Amilibia et al., 2008; Arriagada et al., 2006).

The eastern boundary of the CD is a basement-cored fold related to an east verging reverse fault, which presumably formed during the Jurassic-early Cretaceous (Mpodozis et al., 2005) as part of the extensional Tarapaca basin and was later reactivated. This thick-skinned deformation produced the El Bordo Escarpment where the CD is uplifted over Mesozoic strata of the SA basin (Figure 2). The Barros Arana syncline is the most prominent structure directly east of the El Bordo Escarpment and exposes most of the lower part of the SA basin fill (Figure 2). The geometry of the syncline varies from open and concentric to a tight-

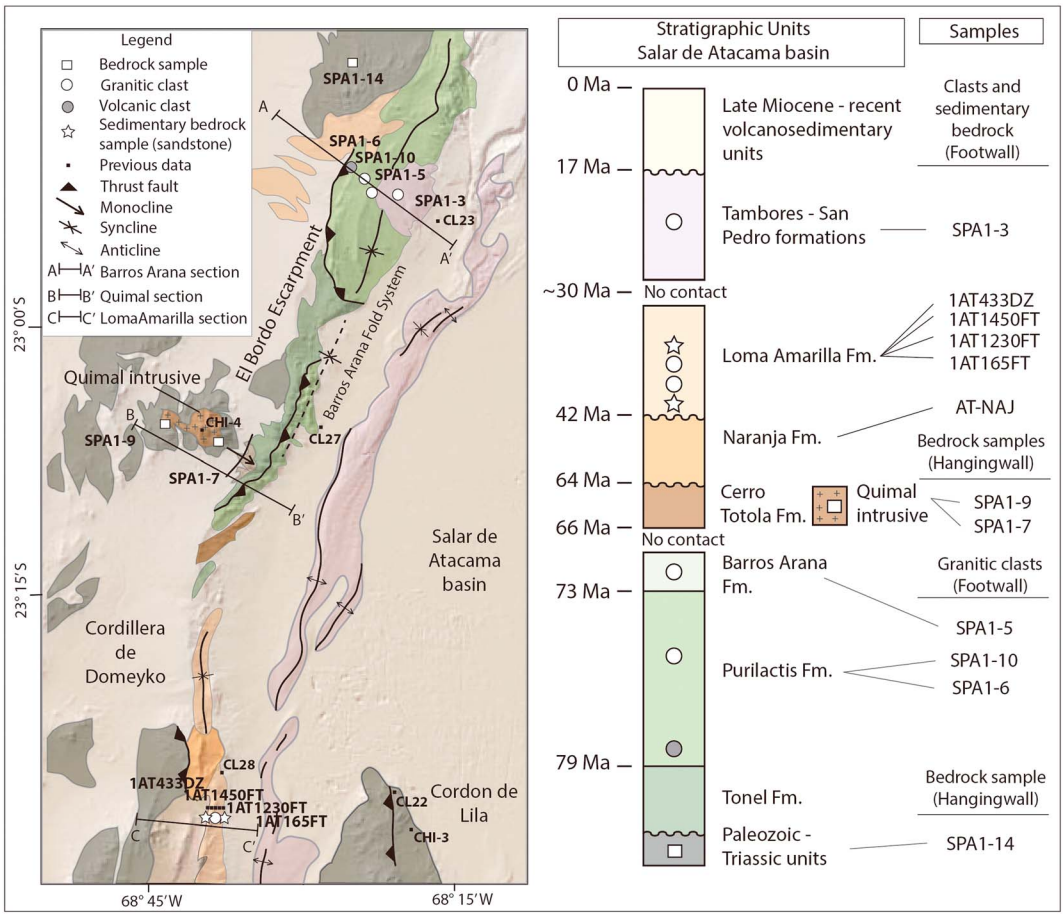

Figure 2. Geologic map of the El Bordo Escarpment, the eastern edge of the Cordillera de Domeyko and western edge of the Salar de Atacama basin (based on Arriagada, 1999), and the stratigraphic units (based on Mpodozis et al., 2005; Jordan et al., 2007). In both parts of the figure, we show the location and type of samples included in this study.

chevron shape (Barros Arana fold system, Figure 2, Arriagada et al., 2006). The structure along the hangingwall of the El Bordo Escarpment also varies along strike, from an east vergent fold formed by a blind fault to a thrust fault (Arriagada et al., 2006).

2.1.2. Stratigraphy of the Salar de Atacama Basin

According to Mpodozis et al., 2005 the SA basin stratigraphy starts with three upper Cretaceous conformable sedimentary formations followed by two Paleogene formations separated by a progressive unconformity (Figure 2). The upper Cretaceous stratigraphy includes the Tonel (460–1,060 m), Purilactis (3,000 m), and Barros Arana (550 m) Formations. Detrital zircon U-Pb data from the Purilactis Formation indicate deposition between ~79 and 73 Ma and the minimum age for the Barros Arana Formation is considered to be pre-66 Ma (Bascuñan et al., 2015). To the south, the Paleocene to middle Eocene Naranja Formation (900 m) was unconformably deposited over lower Paleocene lavas (66–64 Ma, Cerro Totola Formation; Mpodozis et al., 2005). The middle Eocene to early Oligocene Loma Amarilla Formation (2,500 m) was deposited in angular unconformity upon the Naranja Formation and preserves evidence for intraformational syntectonic unconformities (i.e., a progressive unconformity; Mpodozis et al., 2005). The depositional age of the Loma Amarilla Formation is between ~44 and 28 Ma (Mpodozis et al., 2005). During the late Oligocene to early Miocene, the Tambores Formation was deposited on top of the uplifted upper Cretaceous part of the basin fill and the San Pedro Formation was deposited within the basin-proper farther to the east (e.g., Marinovich & Lahsen, 1984; Naranjo et al., 1994). Based on subsurface data the San Pedro Formation is considered to vary in thickness from no less than 3,000 m in the north to 500 m in the south, controlled by an east dipping normal fault (Pananont et al., 2004, and references therein). Thus, this formation marks an extensional episode that started at ~28 Ma in the SA basin and continued until the middle Miocene.

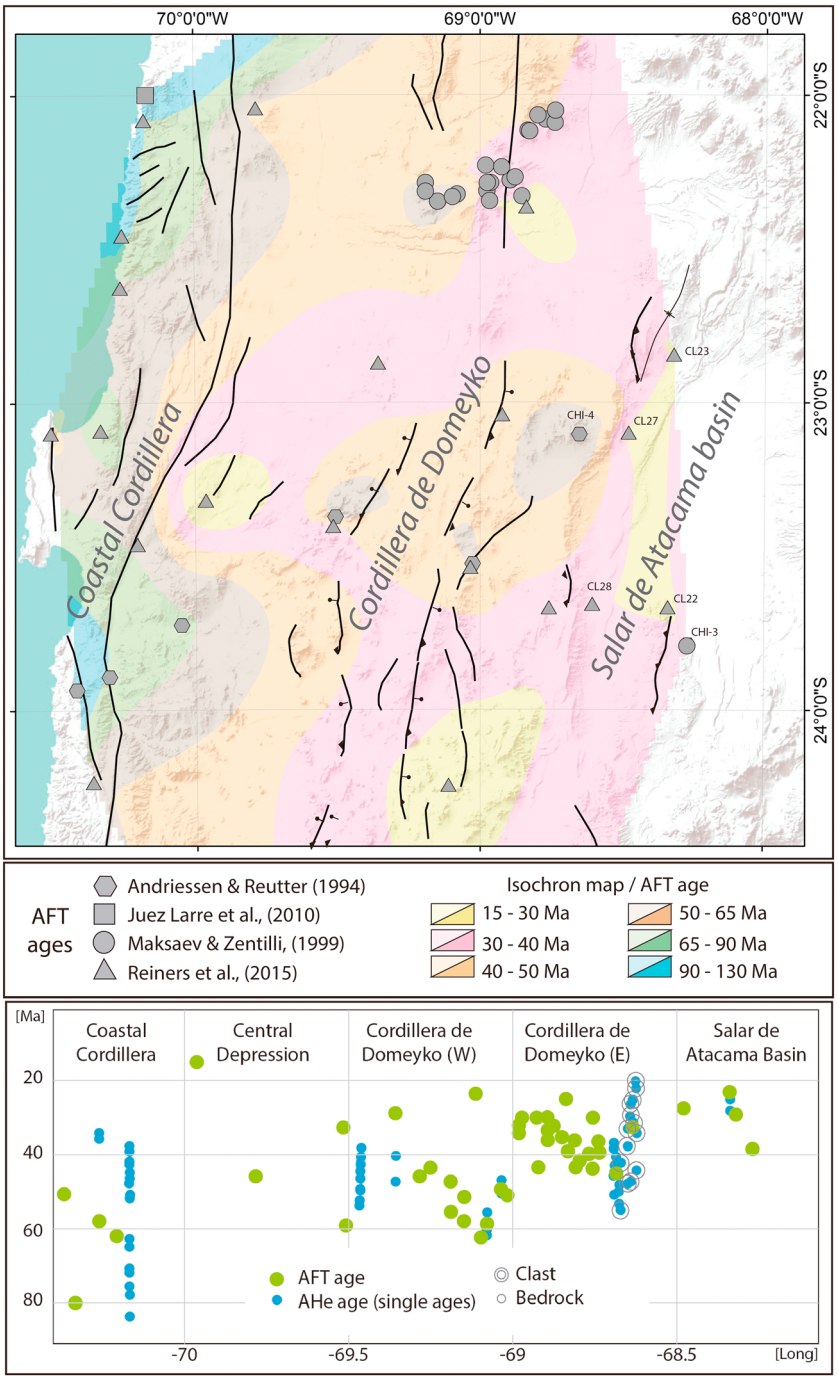

Figure 3. Isochron map based on previous apatite fission track (AFT) bedrock ages. Plot showing the previous AFT and AHe data form clasts and igneous and sedimentary bedrock samples. The six labeled samples (CHI-3, CHI-4, CL22, CL23, CL27, and CL28) are discussed in the text.

2.1.3. Previous Cooling Data From the Modern Forearc

Previous thermochronological studies in the retroarc region at this latitude have produced AFT, AHe, and zircon (U-Th)/He (ZHe) data (Andriessen & Reutter, 1994; Juez-Larré et al., 2010; Maksaev & Zentilli, 1999; Reiners et al., 2015; Figure 3). In the Coastal Cordillera, AHe ages show cooling between ~80 and 60 Ma (Figure 3; Juez-Larré et al., 2010). This cooling postdates the migration of magmatic activity to the east, which was located in the CD by ~80 Ma (e.g., Marinovic & García, 1999). This cooling has been

Table 1
Apatite (U-Th-Sm)/He Data

Sample	Formation	Aliquot name	4He (pmol)	4He (pmol ±1σ)	4He (pmol ±1σ)	U (ng)	U (ng ± 1σ)	Th (ng)	Th (ng ± 1σ)	Sm (ng)
SPA13	Tambores Fm	16A952_SH_CH_SPA1_3_AP1	42482	0.0050	0.0001	0.0064	0.0001	0.0315	0.0005	0.5549
SPA1-3	Tambores Fm	16A953_SH_CH_SPA1_3_AP2	42482	0.0112	0.0002	0.0153	0.0003	0.0482	0.0007	2.1738
SPA1-3	Tambores Fm	16A954_SH_CH_SPA1_3_AP3	42482	0.0136	0.0002	0.0323	0.0005	0.0624	0.0009	0.8225
SPA1-3	Tambores Fm	16A955_SH_CH_SPA1_3_AP4	42482	0.0028	0.0001	0.0066	0.0001	0.0205	0.0004	0.9107
SPA1-3	Tambores Fm	16A956_SH_CH_SPA1_3_AP5	42482	0.0017	0.0001	0.0066	0.0001	0.0116	0.0002	0.3036
SPA1-6	Purilactis Fm	16A963_SH_CH_SPA1_6_AP1	42485	0.0063	0.0001	0.0269	0.0004	0.0737	0.0011	0.6835
SPA1-6	Purilactis Fm	16A964_SH_CH_SPA1_6_AP2	42485	0.0019	0.0001	0.0104	0.0005	0.0268	0.0004	0.2461
SPA1-6	Purilactis Fm	16A965_SH_CH_SPA1_6_AP3	42485	0.0020	0.0000	0.0170	0.0003	0.0193	0.0003	0.2167
SPA1–6	Purilactis Fm	16A966_SH_CH_SPA1_6_AP4	42485	0.0043	0.0001	0.0202	0.0003	0.0518	0.0008	0.5321
SPA1-6	Purilactis Fm	16A967_SH_CH_SPA1_6_AP5	42485	0.0113	0.0001	0.0538	0.0008	0.0879	0.0013	1.7035
SPA1-10	Purilactis Fm	16B881_SH_SPA1_10_1	42599	0.0035	0.0001	0.0136	0.0003	0.0376	0.0005	0.1054
SPA1-10	Purilactis Fm	16B883_SH_SPA1_10_3	42599	0.0300	0.0004	0.1046	0.0015	0.1948	0.0028	1.1728
SPA1-10	Purilactis Fm	16B884_SH_SPA1_10_4	42599	0.0110	0.0002	0.0248	0.0005	0.0689	0.0011	0.5296
SPA1-10	Purilactis Fm	16B885_SH_SPA1_10_5	42599	0.0080	0.0001	0.0229	0.0004	0.0623	0.0009	0.2547
SPA1-7	Quimal Intrusive	16A968_SH_CH_SPA1_7_AP1	42485	0.0055	0.0001	0.0149	0.0002	0.0416	0.0006	0.5921
SPA1-7	Quimal Intrusive	16A969_SH_CH_SPA1_7_AP2	42485	0.0067	0.0001	0.0156	0.0002	0.0419	0.0006	0.5728
SPA1-7	Quimal Intrusive	16A970_SH_CH_SPA1_7_AP3	42485	0.0025	0.0000	0.0097	0.0002	0.0221	0.0003	0.3136
SPA1-7	Quimal Intrusive	16A971_SH_CH_SPA1_7_AP4	42485	0.0030	0.0001	0.0066	0.0001	0.0183	0.0003	0.3040
SPA1-7	Quimal Intrusive	16A972_SH_CH_SPA1_7_AP5	42485	0.0021	0.0001	0.0066	0.0001	0.0163	0.0002	0.2559
SPA1-9	Quimal intrusive	16B876_SH_SPA1_9_1	42599	0.0597	0.0007	0.2422	0.0035	0.2717	0.0039	0.7219
SPA1-9	Quimal intrusive	16B877_SH_SPA1_9_2	42599	0.0358	0.0004	0.1117	0.0016	0.1829	0.0026	0.4587
SPA1-9	Quimal intrusive	16B878_SH_SPA1_9_3	42599	0.0222	0.0003	0.0869	0.0013	0.1553	0.0022	0.3008
SPA1-9	Quimal intrusive	16B879_SH_SPA1_9_4	42599	0.0237	0.0003	0.1090	0.0016	0.1702	0.0025	0.4366
SPA1-9	Quimal intrusive	16B880_SH_SPA1_9_5	42599	0.0795	0.0010	0.2911	0.0042	0.3682	0.0053	0.8252
SPA1-14	Tuina Fm	16B888_SH_SPA1_14_2	42599	0.0165	0.0002	0.0539	0.0008	0.1149	0.0017	1.0386
SPA1-14	Tuina Fm	16B889_SH_SPA1_14_3	42599	0.4385	0.0049	0.1847	0.0027	1.0899	0.0157	5.3959
SPA1-14	Tuina Fm	16B890_SH_SPA1_14_4	42599	0.0118	0.0002	0.0674	0.0010	0.0559	0.0008	0.5591
SPA1-14	Tuina Fm	16B891_SH_SPA1_14_5	42599	0.0318	0.0004	0.1566	0.0023	0.3418	0.0049	1.0659

Note. FT = alpha-ejection correction (see section 3 and references therein); 1 s err anal. = one-sigma analytical precision; eU = equivalent uranium concentration (U + 0.235 × Th); m asl = meters above sea level. WA = weighted average. Aliquot name in cursive was not considered for age.

interpreted to be related to arc uplift and thermal relaxation after the arc left the region. AHe ages from this range show a second period of cooling between ~50 and 40 Ma (Figure 3; Juez-Larré et al., 2010), which the authors explained by erosion of 2.4 km of crust (assuming a forearc geothermal gradient of 20 °C/km).

In the CD, Maksaev and Zentilli (1999) and Reiners et al. (2015) found evidence of cooling since the Paleocene (Figure 3). Maksaev and Zentilli (1999) studied Late Cretaceous intrusions along the CD and argued that they resided between ~350 °C and ~120 °C before 50 Ma. Reiners et al. (2015) suggested that double dated zircons (U-Pb and ZHe) older than ~100 Ma in the Naranja and Loma Amarilla Formations record a nonmagmatic cooling signature. They interpreted the U-Pb and ZHe data as evidence of the progressive unroofing of a volcanic sequence in the CD. Maksaev and Zentilli (1999) identified a period of cooling between ~50 and 30 Ma that can be interpreted to represent exhumation of 4–5 km of rocks from the axis of the CD. Moreover, they suggested that exhumation accelerated between ~40 and 30 Ma. Reiners et al. (2015) found that granitic cobbles from the Loma Amarilla Formation were buried to depths equivalent to the apatite partial retention zone and then exhumed starting at ~20–22 Ma (Figure 3). They argued for erosion of 1.5–3 km of rock from above the Loma Amarilla Formation (<~28 Ma, according to Mpodozis et al., 2005). Burial was probably related to thrusting in the CD before the change to extensional conditions proposed for the area after ~28 Ma (Jordan et al., 2007, and reference therein). To the east, AFT data indicate cooling in the basement of the Cordon de Lila at ~38 Ma (Figure 2; Andriessen & Reutter, 1994).

Synorogenic sedimentation in the SA basin requires correlative exhumation of the CD, which has been poorly understood, especially during the Late Cretaceous and Paleogene. Although cooling during this time is widely documented in the modern retroarc region (Carrapa & DeCelles, 2015, and references therein), the only data available for the CD are from the axis of the range and do not include structures from the thrust belt in the eastern part of the range.

Table 1 *(continued)*

Sample	Sm (ng ± 1σ)	Th/U (atomic)	Raw age (Ma)	Raw age (Ma ± 1σ)	Ft 238 U	Ft 235 U	Ft 232Th	Ft 147Sm	Rs (um)	Corrected age (Ma)	1 s err anal. (Ma)	ppm eU (morph)	ppm U (morph)
SPA13	0.0087	5.0846	63.809	1.215	0.684	0.642	0.642	0.897	44.351	94.862	1.798	6.535	3.019
SPA1-3	0.0339	3.2268	70.685	1.308	0.745	0.710	0.710	0.918	56.056	94.616	1.747	7.903	4.544
SPA1-3	0.0127	1.9827	52.386	0.902	0.762	0.730	0.730	0.924	60.536	69.318	1.195	15.204	10.455
SPA1-3	0.0139	3.2038	41.560	0.943	0.688	0.647	0.647	0.899	45.040	60.172	1.361	6.320	3.645
SPA1-3	0.0047	1.8177	33.311	1.135	0.686	0.644	0.644	0.898	44.639	48.870	1.667	6.847	4.834
SPA1-6	0.0110	2.8137	25.876	0.434	0.736	0.700	0.700	0.915	54.082	35.677	0.599	10.389	6.317
SPA1-6	0.0038	2.6371	21.080	0.873	0.666	0.622	0.622	0.891	41.636	32.304	1.349	9.530	5.941
SPA1-6	0.0035	1.1609	16.676	0.343	0.681	0.639	0.639	0.896	43.932	24.735	0.511	14.090	11.130
SPA1–6	0.0081	2.6302	24.018	0.503	0.722	0.685	0.685	0.910	51.119	33.753	0.707	10.887	6.794
SPA1-6	0.0264	1.6755	27.215	0.344	0.800	0.772	0.772	0.936	72.789	34.200	0.433	14.658	10.593
SPA1-10	0.0022	2.8267	28.299	0.662	0.639	0.592	0.592	0.882	38.153	45.564	1.072	18.259	11.083
SPA1-10	0.0177	1.9106	36.484	0.593	0.789	0.759	0.759	0.932	68.625	46.721	0.761	15.835	11.015
SPA1-10	0.0081	2.8452	48.728	1.014	0.769	0.737	0.737	0.926	62.382	64.206	1.339	8.732	5.286
SPA1-10	0.0038	2.7877	39.003	0.765	0.728	0.691	0.691	0.912	52.281	54.552	1.073	11.906	7.266
SPA1-7	0.0096	2.8660	40.154	0.681	0.729	0.692	0.692	0.913	52.427	55.814	0.947	7.734	4.669
SPA1-7	0.0092	2.7521	47.497	0.761	0.732	0.695	0.695	0.914	53.085	65.718	1.054	7.398	4.538
SPA1-7	0.0048	2.3391	29.839	0.683	0.730	0.694	0.694	0.913	52.804	41.325	0.947	4.897	3.189
SPA1-7	0.0048	2.8266	49.679	1.138	0.717	0.678	0.678	0.909	49.991	70.147	1.608	4.707	2.857
SPA1-7	0.0039	2.5306	35.282	0.994	0.665	0.621	0.621	0.891	41.560	53.829	1.519	6.467	4.094
SPA1-9	0.0108	1.1509	35.934	0.594	0.838	0.816	0.816	0.948	91.138	43.099	0.714	18.010	14.253
SPA1-9	0.0070	1.6798	42.508	0.703	0.769	0.737	0.737	0.926	62.495	55.866	0.928	23.820	17.201
SPA1-9	0.0047	1.8336	33.084	0.572	0.735	0.699	0.699	0.915	53.800	45.663	0.792	29.335	20.658
SPA1-9	0.0065	1.6019	29.242	0.466	0.777	0.746	0.746	0.929	64.713	38.047	0.608	27.029	19.773
SPA1-9	0.0123	1.2976	38.762	0.647	0.806	0.778	0.778	0.938	74.958	48.489	0.812	31.634	24.385
SPA1-14	0.0154	2.1842	36.985	0.622	0.717	0.679	0.679	0.909	50.102	52.297	0.882	35.338	23.553
SPA1-14	0.0830	6.0529	179.190	2.710	0.807	0.780	0.780	0.938	75.530	225.441	3.410	34.460	14.439
SPA1-14	0.0083	0.8515	26.927	0.475	0.670	0.627	0.627	0.893	42.303	40.530	0.718	39.263	32.854
SPA1-14	0.0158	2.2398	24.632	0.389	0.792	0.763	0.763	0.934	69.880	31.466	0.498	39.829	26.323

3. Methods

One of the most useful techniques to constrain exhumation due to erosion is thermochronology. We use AFT and apatite (U-Th)/He (AHe) thermochronology to constrain the cooling history of the CD through the ~120 °C to ~40 °C closure window (e.g., Reiners & Brandon, 2006), which can represent exhumation and erosion in the upper ~4–1 km of the crust (assuming a geothermal gradient of 25 °C/km and a surface temperature of 20 °C). These two thermochronometers have been successfully combined for the same samples (multidating) to determine thermal histories and timing of deformation and exhumation in the Andes (Carrapa et al., 2009; Carrapa & DeCelles, 2015; Reiners et al., 2015). Additionally, we use U-Pb geochronology of zircons to constrain the crystallization age of igneous bedrock samples and of clast source rocks for sedimentary samples (conglomerates), and the maximum depositional age of the sedimentary units investigated (Dickinson & Gehrels, 2009).

3.1. Sampling Strategy

We collected three samples from igneous bedrock along the eastern edge of the CD, which is bounded by a blind east verging reverse fault (Mpodozis et al., 2005; Figures 1 and 2). We also targeted sedimentary units from the SA basin and sampled six granite clasts, three sedimentary bedrock samples (sandstones), and one volcanic clast; the clasts were subrounded cobbles between 18 and 25 cm in diameter. Locations and corresponding stratigraphic positions are shown in Figure 2 and Tables 1 and 2. The three igneous bedrock samples (SPA1-9, SPA1-7, and SPA1-14) belong to the Quimal intrusive and the Tuina Formation. The six granitic clasts (SPA1-3, SPA1-5, SPA1-10, SPA1-6, 1AT1230FT, and 1AT1450FT) are from the Purilactis, Barros Arana, Loma Amarilla, and Tambores Formations. The three sedimentary bedrock samples are from the Cenozoic units, one from the Naranja Formation (AT-NAJ) and two from the Loma Amarilla Formation (1AT165FT and 1AT433DZ). These 12 samples span the upper Cretaceous to early Miocene stratigraphic record.

Table 1 *(continued)*

Sample	ppm Th (morph)	ppm Sm (morph)	nmol 4He/g (morph)	Mass ap (g)	WA age ± σ (Ma)	Standard deviation (Ma)	Standard deviation *100/W.Aage (%)	Longitude (°W)	Latitude (°S)	Elev. (m asl)	Aliquot name	Sample
SPA13	14.962	263.330	2.376	1.737	71.1 ± 0.7	20.6	29.0	−22.776	−68.372	3145	*16A952_SH_CH_SPA1_3_AP1*	SPA1–3
SPA1-3	14.293	644.436	3.333	2.876							*16A953_SH_CH_SPA1_3_AP2*	SPA1-3
SPA1-3	20.206	266.508	4.411	2.300							16A954_SH_CH_SPA1_3_AP3	SPA1-3
SPA1-3	11.384	506.654	1.562	1.409							16A955_SH_CH_SPA1_3_AP4	SPA1-3
SPA1-3	8.565	223.347	1.283	1.137							16A956_SH_CH_SPA1_3_AP5	SPA1-3
SPA1-6	17.326	160.640	1.483	3.717	31.8 ± 0.3	4.3	13.5	−22.701	−68.424	3381	16A963_SH_CH_SPA1_6_AP1	SPA1–6
SPA1-6	15.272	140.509	1.107	1.256							16A964_SH_CH_SPA1_6_AP2	SPA1-6
SPA1-6	12.595	141.444	1.285	1.241							16A965_SH_CH_SPA1_6_AP3	SPA1-6
SPA1–6	17.418	178.921	1.444	2.745							16A966_SH_CH_SPA1_6_AP4	SPA1-6
SPA1-6	17.301	335.239	2.218	4.051							16A967_SH_CH_SPA1_6_AP5	SPA1-6
SPA1-10	30.538	85.575	2.815	1.243	50.6 ± 0.5	8.6	17.0	−22.714	−68.397	3426	16B881_SH_SPA1_10_1	SPA1-10
SPA1-10	20.514	123.528	3.159	9.197							16B883_SH_SPA1_10_3	SPA1-10
SPA1-10	14.661	112.756	2.344	4.299							16B884_SH_SPA1_10_4	SPA1-10
SPA1-10	19.744	80.735	2.538	2.941							16B885_SH_SPA1_10_5	SPA1-10
SPA1-7	13.042	185.589	1.732	2.710	49.4 ± 0.6	7.9	16.0	−23.141	−68.672	3318	16A968_SH_CH_SPA1_7_AP1	SPA1-7
SPA1-7	12.173	166.215	1.958	2.856							*16A969_SH_CH_SPA1_7_AP2*	SPA1-7
SPA1-7	7.271	102.976	0.812	2.565							16A970_SH_CH_SPA1_7_AP3	SPA1-7
SPA1-7	7.872	131.005	1.311	1.915							*16A971_SH_CH_SPA1_7_AP4*	SPA1-7
SPA1-7	10.099	158.603	1.273	1.793							16A972_SH_CH_SPA1_7_AP5	SPA1-7
SPA1-9	15.990	42.488	3.513	7.793	44.6 ± 0.3	6.6	14.8	−23.078	−68.713	3386	16B876_SH_SPA1_9_1	SPA1-9
SPA1-9	28.165	70.619	5.506	5.116							16B877_SH_SPA1_9_2	SPA1-9
SPA1-9	36.923	71.536	5.271	3.308							16B878_SH_SPA1_9_3	SPA1-9
SPA1-9	30.875	79.216	4.293	4.863							16B879_SH_SPA1_9_4	SPA1-9
SPA1-9	30.844	69.122	6.656	11.231							16B880_SH_SPA1_9_5	SPA1-9
SPA1-14	50.147	453.408	7.191	2.179	37.6 ± 0.4	10.4	27.7	−22.537	−68.437	3151	16B888_SH_SPA1_14_2	SPA1-14
SPA1-14	85.194	421.796	34.279	12.429							*16B889_SH_SPA1_14_3*	SPA1-14
SPA1-14	27.270	272.586	5.763	1.756							16B890_SH_SPA1_14_4	SPA1-14
SPA1-14	57.472	179.212	5.340	3.625							16B891_SH_SPA1_14_5	SPA1-14

3.2. U-Pb Geochronology

U-Pb detrital zircon geochronology by means of laser ablation inductively coupled plasma mass spectrometry following the method described by Gehrels et al. (2008) is here used to constrain the maximum depositional ages of the Paleogene deposits and to assess sediment provenance. Age peaks and populations were calculated using the Excel spreadsheet *Age Pick* program provided by the LaserChron Center at the University of Arizona (https://sites.google.com/a/laserchron.org/laserchron/). We used the youngest cluster with three or more grains ages to constrain the maximum depositional age (Dickinson & Gehrels, 2009). Additionally, four granitic clasts were dated by zircon U-Pb geochronology (SPA1-3, SPA1-5, SPA1-10, and 1AT1230FT) to compare their crystallization ages with the cooling ages obtained with AFT and/or AHe techniques. This helps to determine if the cooling signature is related to magmatic activity or tectonic-erosional processes (Table S1, in the supporting information).

3.3. Thermochronology

3.3.1. Apatite (U-Th)/He Thermochronology

(U-Th)/He thermochronology of apatite uses the concentration of ^{4}He formed by alpha decay of U, Th, and Sm, which is largely retained in apatite crystals at temperatures below ~70 °C and is lost by diffusion at higher temperatures (e.g., Farley, 2000). Radiogenic He produced by an apatite experiencing cooling starts to be retained within the crystal at temperatures between ~40 and 70 °C, the so-called partial retention zone.

We analyzed five single apatite grains per sample in the Arizona Radiogenic Helium Dating Laboratory at the University of Arizona. The (U-Th)/He crystal ages were obtained using a two-stage analytical procedure where first the crystal is degassed by heating to measure the gas ^{4}He using gas source mass spectrometry, and then the parent nuclides (U, Th, and Sm) are measured using inductively coupled plasma mass spectrometry (Reiners & Nicolescu, 2006). To analyze the results, we first addressed morphology issues and the presence of

Table 2
Apatite Fission Track Data

Sample	Unit	Type	No. of crystals	Spontaneous		Induced		$P(\chi)2$ (%)	Dosimeter		Age pooled (Ma± 1σ)	Age central (Ma ± 1σ)	Longitude (°W)	Latitude (°S)	Elevation (m asl)
				ρ_s	N_s	ρ_i	N_i		ρ_d	N_d					
1AT1230FT	Loma Amarilla Fm.	Granitic clast	17	1.6	98	1.2	773	99.37	25.3	4398	56.7 ± 6.4	56.7 ± 6.4	−68.639	−23.719	2,765
1AT1450FT	Loma Amarilla Fm.	Granitic clast	17	2	132	5.4	354	99.5	26.1	4398	170.1 ± 18.4	170.1 ± 18.4	−68.642	−23.721	2,815
SPA1-9	Quimal intrusive	Bedrock	20	1.8	126	6.8	473	97.91	12.8	4604	60.2 ± 6.4	60.2 ± 6.4	−68.713	−23.078	3,386
SPA1-7	Quimal intrusive	Bedrock	12	0.63	25	3.3	132	99.4	12.1	4604	40.5 ± 9	40.5 ± 9	−68.672	−23.141	3,318
SPA1-10	Purilactis Fm.	Granitic clast	17	1.6	38	4.8	127	99.9	13.8	4604	72.6 ± 13.7	72.6 ± 17.3	−68.397	−22.714	3,426
SPA1-5	Barros Arana Fm.	Granitic clast	14	1.4	60	3.9	141	61.96	13.9	4604	104.8 ± 16.6	104.8 ± 16.9	−68.395	−22.750	3,374
SPA1-3	Tambores Fm.	Granitic clast	9	0.87	13	2.6	39	91.8	13.2	4604	77.4 ± 25	77.4 ± 25	−68.372	−22.776	3,145
1AT165DZ	Loma Amarilla Fm.	Sedimentary bedrock	100	0.58		4.3		48.96	26.3	4398		NA	−68.627	−23.715	2,659
1AT433DZ	Loma Amarilla Fm.	Sedimentary bedrock	100	1.1		5.9		0.00	26.4	4398		NA	−68.648	−23.718	2,847

Note. ρ_s = spontaneous track density ($\times 10^5$), N_s = number of spontaneous tracks; ρ_i = induced track density ($\times 10^5$); Ni—number of induced tracks; ρ_d—dosimeter track density ($\times 10^5$); N_d = number of dosimeter tracks; $P(\chi)2 = \chi 2$ probability; m asl = meters above sea level. Error is 1σ, calculated using the zeta calibration method (Hurford & Green, 1983) with zeta of 354.7 ± 11.7 for apatite.

inclusions. Then we explored possible correlations between AHe age, effective uranium concentration (eU), and equivalent spherical radius (Rs) using different single aliquots from each sample (supporting information Figures S5 and S6; e.g., Flowers, 2009). Finally, we considered He implantation for grains with low U content, for small grains (<40 μm; Gautheron et al., 2012) producing anomalously old ages and for grains with cooling ages older than the crystallization age and which do not show clear age-eU relationships.

3.3.2. AFT Thermochronology

Fission tracks are formed by spontaneous fissioning of ^{238}U. Fission tracks in apatite crystals are preserved at temperatures below ~60 °C, partially annealed between ~60 °C and ~120 °C within the partial annealing zone (Gleadow et al., 1986) and fully annealing at higher temperatures. The closure temperature of the AFT system strongly depends on the kinetic characteristics of the apatites and the cooling rate (e.g., Ketcham et al., 1999, and references therein).

The apatite separates were mounted in epoxy, polished, etched in 5.5 M nitric acid for 20 s at 21 °C, according to methods outlined by Donelick et al. (2005), and irradiated at Oregon State University on glass slides. After irradiation, the mica prints were etched in 49% hydrofluoric acid for 15 min at 23 °C following the protocol described by Donelick et al. (2005). Fission tracks were counted by optical identification using an Olympus petrographic microscope at 1600X magnification at the University of Arizona. According to generally accepted practices, AFT age determinations are based on 20 grains per bedrock sample or granite cobble and 100 grains per sedimentary bedrock sample selected randomly and dated using the external detector method (Hurford & Green, 1982). In samples that lacked these numbers of suitable grains, we counted all suitable grains. For sedimentary bedrock samples, detrital populations (of grains cooled before their deposition and therefore thermally not reset) were calculated using the automatic mixture modeling algorithm implemented in the java application *RadialPlotter* (Vermeesch, 2009).

4. Results

4.1. U-Pb Geochronology Results

The U-Pb zircon ages from the two sedimentary bedrock samples are shown in Table 3 and in the data Table S1 (supporting information). The Naranja Formation (AT-NAJ, Figure 4) produced a youngest age population of 73.7 ± 1 Ma. The Loma Amarilla Formation (1AT433DZ, Figure 4) yielded a youngest population age of 42.4 ± 0.8 Ma.

The four granitic clasts yielded Permian to Triassic U-Pb zircon ages (Tables 3 and S1 in the supporting information). The two clasts from the upper Cretaceous units produced U-Pb ages of 295.2 ± 2.1 Ma (SPA1-10) and 288.7 ± 2.3 Ma (SPA1-5). The clast from the Loma Amarilla Formation produced a U-Pb zircon age of 234.7 ± 2.8 Ma (1AT1230FT) and the clast from the Tambores Formation an age of 296.3 ± 2.2 Ma (SPA1-3).

4.2. Apatite (U-Th)/He Thermochronology

A total of 28 single apatite grains from six samples were analyzed using (U-Th)/He thermochronology. The AHe data are shown in Table 1 and sample locations are shown on Figure 2. To analyze the results, we first looked for correlations between eU-Rs and eU-corrected age (supporting information Figures S5 and S6). Correlations between these parameters indicate radiation damage (e.g., Flowers, 2009; Shuster et al., 2006). We rejected grains with cooling ages older than the crystallization age for the same sample. Grains from igneous samples with cooling ages equal to crystallization ages (within error) are reported, but because they record the magmatic cooling, they were not used for interpretation about the exhumation-related cooling history. Results from two grains, one from sample SPA1-10 and another from sample SPA1-14, were not reported because they are not from apatite; three other grains, from samples SPA1-7 and SPA1-14, are not considered due to ages equal to or older than crystallization ages. The remaining data were analyzed using the weighted

Table 3
Summary of the New Geochronologic and Thermochronologic Ages

Sample/type	Depositional/formation/ crystallization age	U-Pb age (Ma)	AFT age (Ma)	AHe age (Ma)	AHe age Standard deviation (Ma)	Observations
SPA1-6/volcanic clast	79–73 Ma/Purilactis Fm. /Bascuñan et al. (2015)	NA	NA	31.8 ± 0.3	4.3	Thermally reset for AHe system (T > ~70 °C) The hangingwall of a west-verging thrust fault detached on the evaporates of the Tonel Formation (e.g., Mpodozis et al., 2005).
SPA1-10/granite clast	79–73 Ma/Purilactis Fm. /Bascuñan et al. (2015)	295.2 ± 2.1	72.6 ± 13.7	50.6 ± 0.5	8.6	The AFT age is, within error, contemporaneous with the deposition of the Purilactis Formation. The AHe age shows a later reheating that at least partially reset the AHe system (see text)
SPA1-5/granite clast	73–66 Ma/Barros Arana Fm. /Bascuñan et al. (2015)	288.7 ± 2.3	104.8 ± 16.6	NA	NA	Paleozoic source cooled during the early Cretaceous
SPA1-3/granite clast	28–14 Ma/Tambores Fm. /Naranjo et al. (1994)	296.3 ± 2.2	77.4 ± 25	71.1 ± 0.7	20.6	Paleozoic source cooled during the Late Cretaceous to Paleocene and not buried enough as for resetting the AFT or AHe age after its deposition
SPA1-14/bedrock	236,3 ± 2,5 Ma/Tuina Fm. / Henriquez et al. (2014)	NA	NA	37.6 ± 0.4	10.4	
SPA1-7/bedrock	64–66 Ma; Basso and Mpodozis (2012)	NA	40.5 ± 9	49.4 ± 0.6	7.9	Two thermochronologic ages within error suggesting fast cooling through the ~120–70 °C closure temperature window
SPA1-9/bedrock	64–66 Ma/Quimal Intrusive/Basso and Mpodozis (2012)	NA	60.2 ± 6.4	44.6 ± 0.3	6.6	The AFT age is, within error, contemporaneous with the crystallization of the Quimal intrusive
1AT1230FT/granite clast	44–28 Ma/Loma Amarilla Fm. /Mpodozis et al. (2005)	234.7 ± 2.8	56.7 ± 6.4	NA	NA	Triassic source cooled during the Paleocene
1AT1450FT/granite clast	44–28 Ma/Loma Amarilla Fm. /Mpodozis et al. (2005)	NA	170.1 ± 18.4	NA	NA	Source cooled during the Jurassic
1AT165FT/sedimentary bedrock	44–28 Ma/Loma Amarilla Fm. /Mpodozis et al. (2005)	NA	*64 ± 5.1	NA	NA	No reset for AFT system
1AT433DZ/sedimentary bedrock	44–28 Ma/Loma Amarilla Fm. /Mpodozis et al. (2005)	NA	*81.9 ± 8.8	NA	NA	No reset for AFT system

Note. AFT = apatite fission track; NA = Not Applicable; * = Age of population in sedimentary bedrock sample.

mean and the standard deviation, both expressed in Ma in Table 1. A high ratio of (standard deviation×100)/(weighted mean age) indicates high variability in the data set. This is the case for samples SPA1-3 and SPA1-14, where this ratio exceeded 20% (scattered ages around the mean value). We describe the results for each sample in the following section.

The bedrock sample from the Triassic unit (SPA1-14) has eU concentrations between 34 and 39 ppm and cooling ages between 31.4 ± 0.4 and 225.4 ± 3.4 Ma. One grain that produced a Triassic (~225 Ma) age similar to its depositional age (236.3 ± 2.5 Ma, zircon U-Pb, Henríquez et al., 2014) was excluded from the weighted mean calculation and standard deviation. The other three grains show no clear correlations among age, eU, and Rs. The weighted mean value for these three cooling ages is 37.6 ± 0.4 Ma and the standard deviation 10.4 Ma.

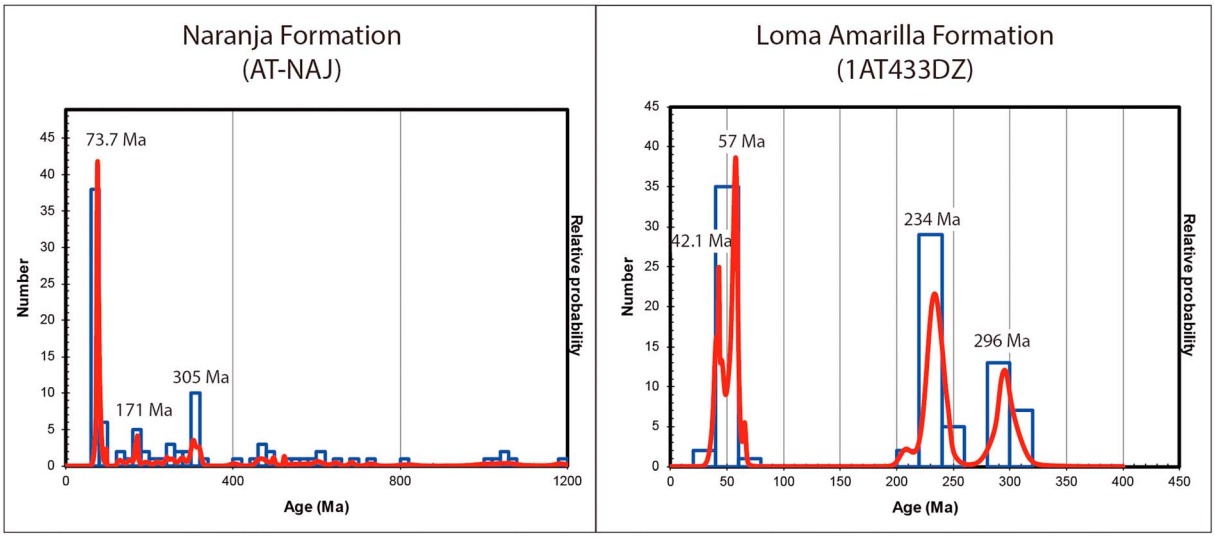

Figure 4. U-Pb detrital zircon ages for the Naranja and Loma Amarilla Formations. The youngest peak for the Naranja Formation is 73.7 ± 1 Ma (38 grains), while the youngest peak for the Loma Amarilla Formation is 42.4 ± 0.8 Ma (14 grains).

The easternmost sample from the Quimal intrusive (SPA1-7) has eU concentration between 4.7 and 7.7 ppm and cooling ages between 41.3 ± 0.9 Ma and 70.1 ± 1.6 Ma. One grain has an age similar to the crystallization age of the intrusive (SPA1-7-AP2 in Tables 1, 66–64 Ma, Basso & Mpodozis, 2012), whereas a second grain (SPA1-7-AP4 in Table 1) is much older than the other grains (SPA1-7-AP1, SPA1-7-AP3, and SPA1-7-AP5 in Table 1), suggesting possible He implantation. The weighted mean of the remaining three grains

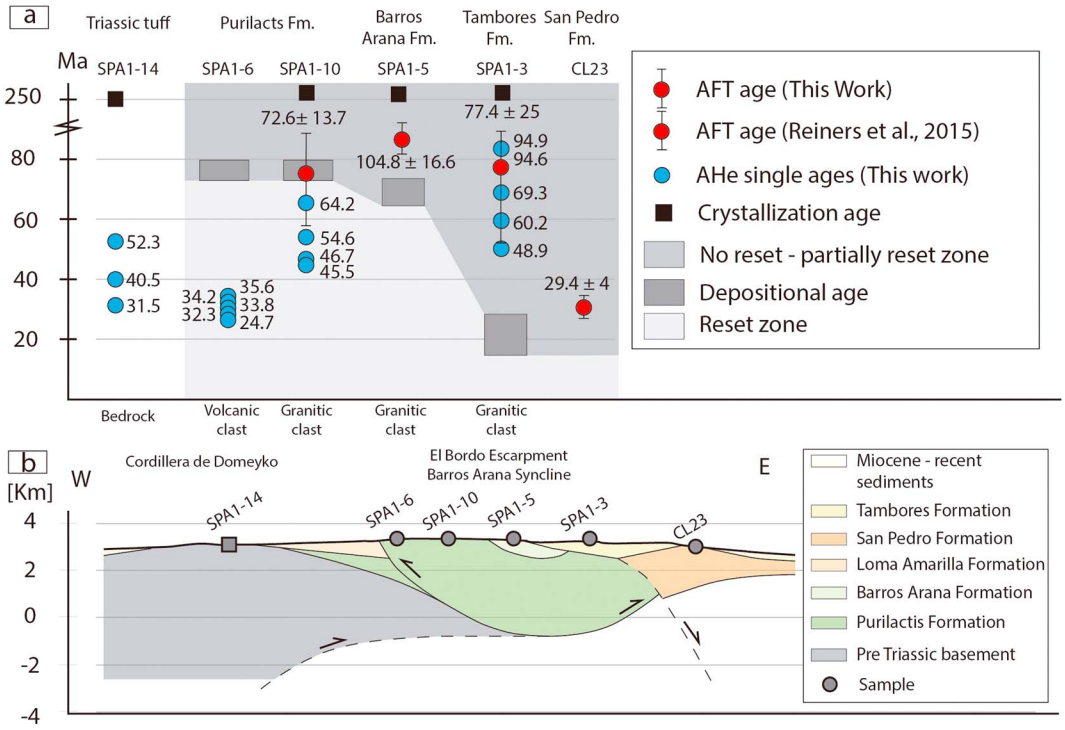

Figure 5. Thermochronological results for the Barros Arana section. The trace of the section is shown in the Figure 2. (a) Plot of apatite fission track (AFT), AHe, crystallization, and/or depositional age for each sample. The *reset zone* separates cooling ages younger than the deposit; therefore, they reflect a cooling event after a reheating episode that reset the previous cooling signal. Conversely, the cooling ages in the *no reset—partially reset zone* show the cooling signal predeposition of the clast, that is, the cooling history of the source. (b) Schematic section showing the location of the samples. Based on interpretations of Arriagada et al. (2006) and Jordan et al. (2007).

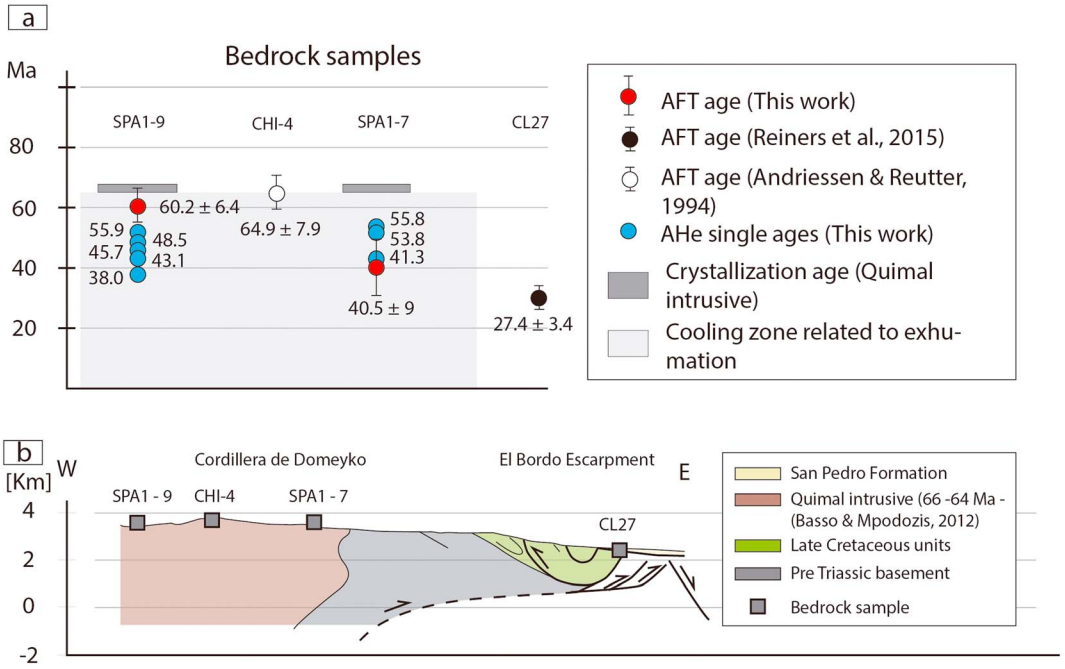

Figure 6. Thermochronological results for Quimal section. The trace of the section is shown in the Figure 2. (a) Plot of apatite fission track (AFT), AHe, and crystallization age for basement samples. (b) Schematic section showing the location of the samples. Modified from Arriagada et al. (2006).

is 49.4 ± 0.6 Ma and the standard deviation of 7.9 Ma. The westernmost sample from the same intrusive body (SPA1-9) has eU concentrations between 18 and 31 ppm and has cooling ages between 38 ± 0.6 and 55.9 ± 0.9 Ma, with a weighted mean of 44.6 ± 0.3 Ma and a standard deviation of 6.6 Ma.

The sample at the base of the Purilactis Formation (SPA1-6) has eU concentration between 9 and 14 ppm and ages between 24.7 ± 0.5 and 35.6 ± 0.6 Ma with a weighted mean age of 31.8 ± 0.3 Ma and a standard deviation of 4.3 Ma. The sample in the middle of the stratigraphic section (SPA1-10) has eU concentrations between 7 and 18 ppm and produced ages between 45.5 ± 1.1 and 64.2 ± 1.3 Ma. The grains with lower eU correlate with older cooling ages, but they show no correlation between Rs and the age; we report the weighted mean age of the four grains (50.6 ± 0.5 Ma) and the standard deviation (8.6 Ma). The sample from the Tambores Formation (SPA1-3) has eU concentrations between 6.5 and 15 ppm and cooling ages between 48.9 ± 1.7 and 94.9 ± 1.8 Ma with a weighted mean age of 71.1 ± 0.7 and a standard deviation of 20.6 Ma. These grains have no clear correlation between age, eU, and Rs. We note that the large standard deviation for this sample (20.6 Ma, Table 1) possibly indicates a mixed cooling signal.

4.3. Apatite Fission Track Thermochronology

Nine samples were analyzed for AFT thermochronology: two bedrock samples, five granitic clasts, and two sandstones (sedimentary bedrock). The AFT data are shown in Table 2 and sample locations are shown in Figure 2. All samples pass χ^2 test indicating homogeneous populations (e.g., Galbraith, 2005; Green, 1981). We report the pooled ages (Ma ± 1σ, Table 2).

AFT cooling ages range from 40.5 ± 9 to 170 ± 18.4 Ma. The bedrock samples from the eastern side of the CD are from an early Paleocene intrusive in the central part of the basin (samples SPA1-7 and SPA1-9, Quimal intrusive; Figure 6). Sample SPA1-9 has an AFT age of 60.2 ± 6.4 Ma and sample SPA1-7 of 40.5 ± 9 Ma. The granitic clast from the Purilactis Formation produced and AFT age of 72.6 ± 13.7 Ma (SPA1-10), whereas the granitic clast from the Barros Arana Formation has an age of 104.8 ± 16.6 Ma (SPA1-5). The granitic clasts from the Loma Amarilla Formation shows ages between 56.7 ± 6.4 Ma (1AT1230FT) and 170.0 ± 18.4 Ma (1AT1450FT). These clasts are ~300 m apart in the stratigraphic column. The granitic clast from the Tambores Formation has an age of 77.4 ± 25 Ma (SPA1-3). The two sedimentary bedrock samples from

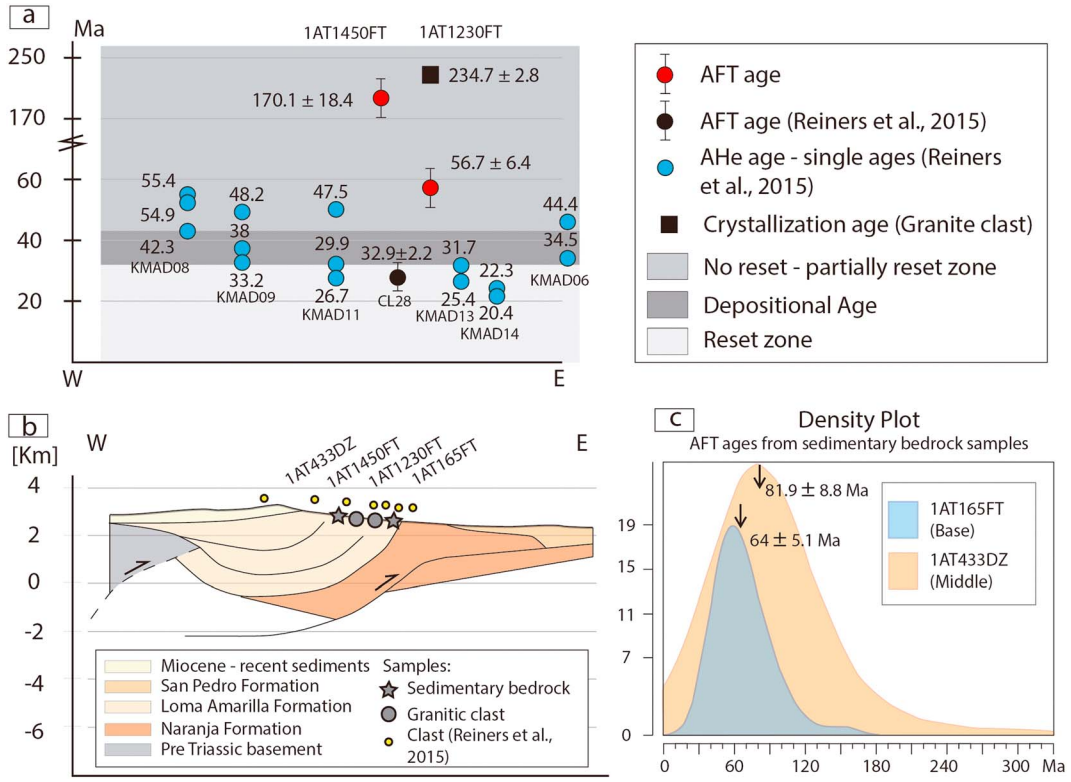

Figure 7. Thermochronological results for the Loma Amarilla section. The trace of the section is shown in the Figure 2. (a) Plot of apatite fission track (AFT), AHe, crystallization, and/or depositional age for each clast analyzed from the Loma Amarilla Fm. The reset zone separates cooling ages younger than the deposit; therefore, they reflect a cooling event after a reheating episode that reset the previous cooling signal. Conversely, the cooling ages in the no reset—partially reset zone show the cooling signal predeposition of the clast, that is, the cooling history of the source. (b) Schematic section showing the location of the samples. Samples from Reiners et al. (2015) are located in the same relative positions both in the plot and in the EW section. (c) Density plot and younger age pick for the two sedimentary bedrock samples (96 grains for the sample 1AT165FT and 100 grains for the sample 1AT433DZ). Density plots made using the software DensityPlotter (Vermeesch, 2009), which found one population in each sample.

the Loma Amarilla Formation show one main population. Sample 1AT165DZ (95 grains, Figure 7) shows a youngest population of 64 ± 5.1 Ma, and sample 1AT433DZ (100 grains, Figure 7) shows a youngest population of 81.9 ± 8.8 Ma. Two granitic clasts have few apatite grains (12 in the sample SPA1-7 and 9 in the sample SPA1-3) and large relative errors (40.5 ± 9 and 77.4 ± 25 Ma, respectively); nevertheless, both samples passed the chi-square test (Table 2), so we carefully considered them in our interpretations.

5. Exhumation of the Eastern Cordillera de Domeyko

The CD is a thermally complex region owing to the influence of Late Cretaceous to Eocene magmatism. Cooling in this region could have been caused by deformation-driven exhumation and/or erosion, cooling following magmatism, and/or a decrease in the geothermal gradient. Reheating could reflect structural or sedimentary burial and/or an increase in the geothermal gradient. In the absence of geothermal gradient measurements in the CD, we rely on published ranges for geothermal gradients in Andean forearc, magmatic arc, and retroarc regions (Giese, 1994; Rothstein & Manning, 2003). Based on this, we assumed a geothermal gradient of 40 °C/km for samples that cooled in the CD before the end of magmatism in the region (at ~37 Ma; samples SPA1-3, SPA1-5, SPA1-10, SPA1-14, 1AT1230FT, and 1AT1450FT) or near the Quimal intrusive during its magmatic cooling (SPA1-7 and SPA1-9, Figures 2 and 6); and a geothermal gradient of 30 °C/km for samples that we know were not close to magmatic bodies (SPA1-7 and SPA1-9 after the magmatic cooling of the intrusive and SPA1-6, Figures 2, 5, and 6). We assumed that the mean surface temperature for all samples was 20 °C.

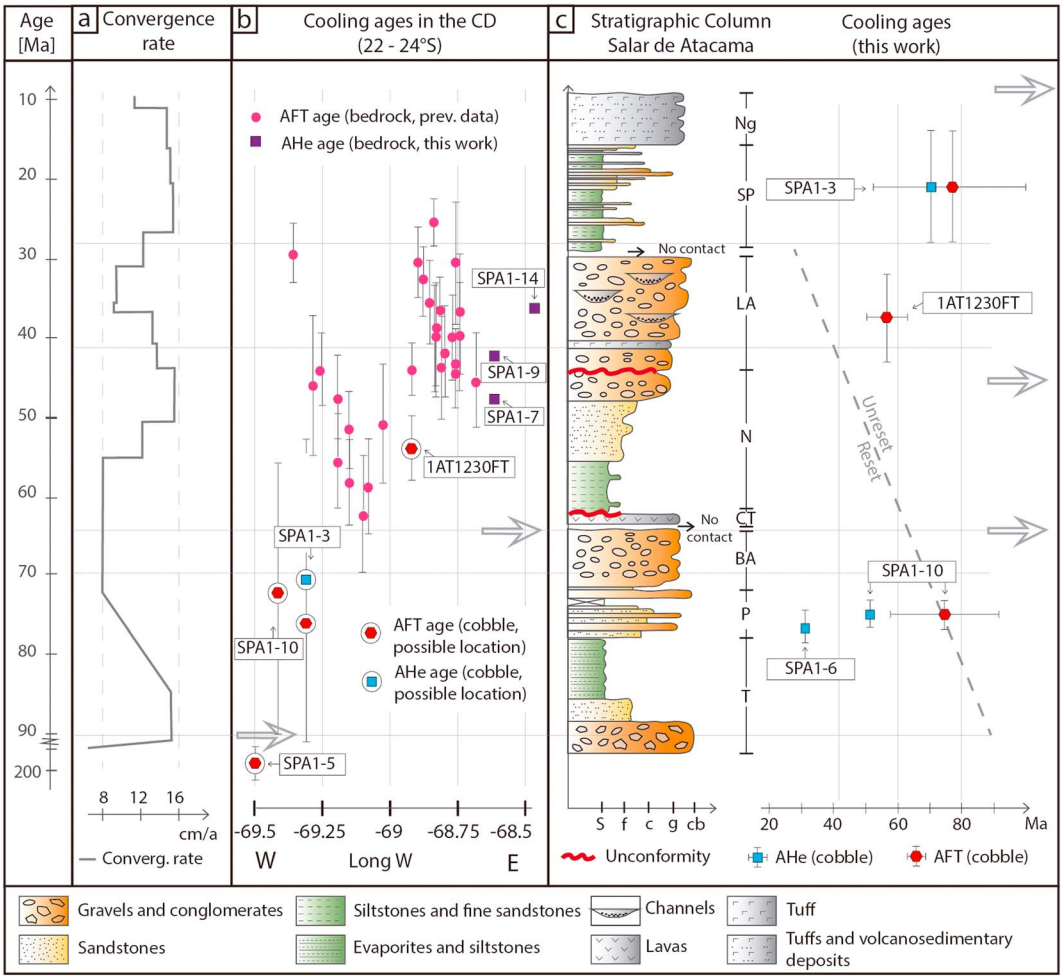

Figure 8. The figure summarizes local and regional processes in the Andes between 22° and 24°S. (a) Convergence rates from Pardo-Casas and Molnar (1987) and Soler and Bonhomme (1990). (b) Apatite fission track (AFT) ages (Andriessen & Reutter, 1994; Maksaev & Zentilli, 1999; Reiners et al., 2015) and AHe ages from this work. To avoid possible cooling signal due to magmatism, only AFT ages (plus analytical error) 10 Ma or younger than the corresponding crystallization age were plotted. The previous AHe ages were not included because of the age dispersion within each sample and without a single cooling history or meaning for them. Additionally, this graph contains the possible location of the cobble samples (from the basin) in the source area (Cordillera de Domeyko). (c) Stratigraphic section for the Salar de Atacama basin (after Wilkes & Görler, 1994; Mpodozis et al., 2005; Bascuñan et al., 2015) and cooling ages from this work. Ng = Neogene deposits; SP = San Pedro and Tambores Formations; LA = Loma Amarilla Formation; N = Naranja Formation; CT = Cerro Totola Formation; BA = Barros Arana Formation; P = Purilactis Formation; T = Tonel Formation. The horizontal arrows show times when the deformation front migrated to the east and their relative position with respect to the CD and Salar de Atacama basin.

Our new thermochronological data show cooling from Late Cretaceous to Oligocene time. Thermochronological ages recorded in the stratigraphic units sampled in this study show both predepositional and postdepositional cooling ages, which indicate a mixed signal including cooling of the source terrane, some degree of thermal resetting during burial (or magmatic heating), and subsequent basin cooling (by exhumation). Ages and corresponding interpretations are compiled in Table 3, shown in the Figures 5, 6 and 7, and discussed below in the context of each section and from higher to lower temperature systems.

5.1. Barros Arana Section

Three granitic cobbles from the Purilactis, Barros Arana and Tambores formations (~79–73 Ma, ~73–66 and late Oligocene to early Miocene, respectively) were multidated (SPA1-10, SPA1-5, and SPA1-3; U-Pb, AFT, and AHe). The zircon U-Pb ages are all Permian (295.2 ± 2.1, 288.7 ± 2.3, and 296.3 ± 2.2 Ma, respectively). These ages in the Upper Cretaceous sequence represent erosion of a Permian source terrane during

deposition. The AFT ages from samples SPA1-10, SPA1-3, and SPA1-5 show cooling since at least ~86 Ma and as early as 104.8 ± 16.6 Ma (Figures 5 and 8c). AFT cooling ages of samples SPA1-5 and SPA1-3 record exhumation during the Lower or Upper Cretaceous; however, sample SPA1-10 (located at a lower stratigraphic position) shows cooling during the Upper Cretaceous. The AFT age from sample SPA1-10 (72.6 ± 13.7 Ma) indicates a cooling event prior to its deposition in the Purilactis Formation that ended at 73 Ma. We interpret this cooling signal to be related to exhumation associated with deformation (shortening). This interpretation requires exhumation of at least ~2.5 km (assuming a geothermal gradient of 40 °C/km) during deposition of the Purilactis Formation.

Sample SPA1-14 shows cooling during the late Eocene (AHe age, 37.6 ± 0.4 Ma, with a standard deviation of 10.4 Ma, Table 1 and Figures 2 and 5), which we interpret as exhumation of the Triassic section in the eastern basement uplift of the CD (Figure 2). The samples from the upper Cretaceous to Miocene sedimentary sections (SPA1-6, SPA1-10, SPA1-5, and SPA1-3) show progressively younger AHe ages from stratigraphically top to bottom (Figure 5) indicating varying degrees of burial heating and subsequent basin cooling. The volcanic clast at the base of the Purilactis Formation was thermally reset at ~32 Ma (AHe age, SPA1-6, with a standard deviation of 4.3 Ma). We interpret this age as cooling driven by exhumation and erosion of ~1.6 km (assuming 30 °C/km and a mean surface temperature of 20 °C) of rocks between ~32 Ma and middle Miocene time when the Tambores Formation accumulated unconformably on top of the previously deformed Barros Arana syncline (Figures 2 and 5). The section removed to reset the AHe ages is the part of the Purilactis Formation located above the sample (SPA1-6) which was later accumulated in the SA basin (Tambores or San Pedro formations). Moreover, in this context, we interpret the AHe from the granitic cobble (SPA1-10, 50.6 ± 0.5 Ma, with a standard deviation of 8.6 Ma,), located ~1.5 km up-section, to represent a mixed age due to partial resetting after deposition. This age further supports cooling due to the exhumation of a Permian source during the Late Cretaceous, as suggested by the aforementioned AFT ages. Father east, an AFT age reported by Reiners et al. (2015) shows Oligocene cooling (CL23, 29.4 ± 4 Ma, Figure 3). This sample was originally interpreted to belong to the Naranja Formation; however, according to the geologic map (Henríquez et al., 2014), it probably belongs to the Oligo-Miocene San Pedro Formation. If so, the AFT age is older than the unit therefore it represents cooling in the source.

5.2. Quimal Section

In the Quimal section, two igneous samples from the Quimal intrusive (~66–64 Ma, Figure 6) were dated with AFT and AHe thermochronology. The AFT ages show cooling at 60.2 ± 6.4 (SPA1-9) and 40.5 ± 9 Ma (SPA1-7). Sample SPA1-9 has an AFT cooling age within range of the crystallization age of the Quimal intrusive, so we interpret this age to represent magmatic cooling. This implies that the intrusive had to be emplaced at a depth at least equivalent to the closure temperature for the AFT system (~120 °C). Sample SPA1-7 has an AFT age within range of the AHe age, suggesting fast cooling through the ~120–70 °C temperature window.

AHe ages from samples SPA1-9 and SPA1-7 indicate cooling between 49.4 ± 0.6 (standard deviation of 7.9 Ma) and 44.6 ± 0.3 Ma (standard deviation of 6.6 Ma). We interpret these ages to be related to exhumation during the middle Eocene. Thus, the AFT (SPA1-7) and AHe data (SPA19 and SPA1-7) suggest erosion of ~3.3 km of rocks between 50 and 28 Ma, with at least ~1.6 km of rocks eroded between ~50 and 40 Ma and a maximum of ~1.7 km between ~40 and 28 Ma (assuming a geothermal gradient of 30 °C/km and a mean surface temperature of 20 °C). An unconformity beneath Eocene-Oligocene strata, which rest on top of Triassic to Eocene units both in the axial part of the CD (Calama Basin, Figure 1, May et al., 2005) and in the eastern part of the CD (Mpodozis et al., 2005), provides a temporal constraint on the time when the samples reached the surface. Considering this, the AFT (SPA1-7) and AHe data (SPA19 and SPA1-7) suggest erosion of ~3.3 km of rocks between 50 and 28 Ma, with at least ~1.6 km of rocks eroded between ~50 and 40 Ma and a maximum of ~1.7 km between ~40 and 28 Ma (assuming a geothermal gradient of 30 °C/km and a mean surface temperature of 20 °C). East of the El Bordo Escarpment, a sedimentary bedrock sample from the Purilactis Formation by Reiners et al. (2015), shows an AFT cooling age of 27.4 ± 3.4 Ma (CL27; Figures 3 and 6). This cooling age can potentially be explained by tectonic exhumation due to the extensional episode proposed for the Oligo-Miocene (e.g., Pananont et al., 2004; Rubilar et al., 2017).

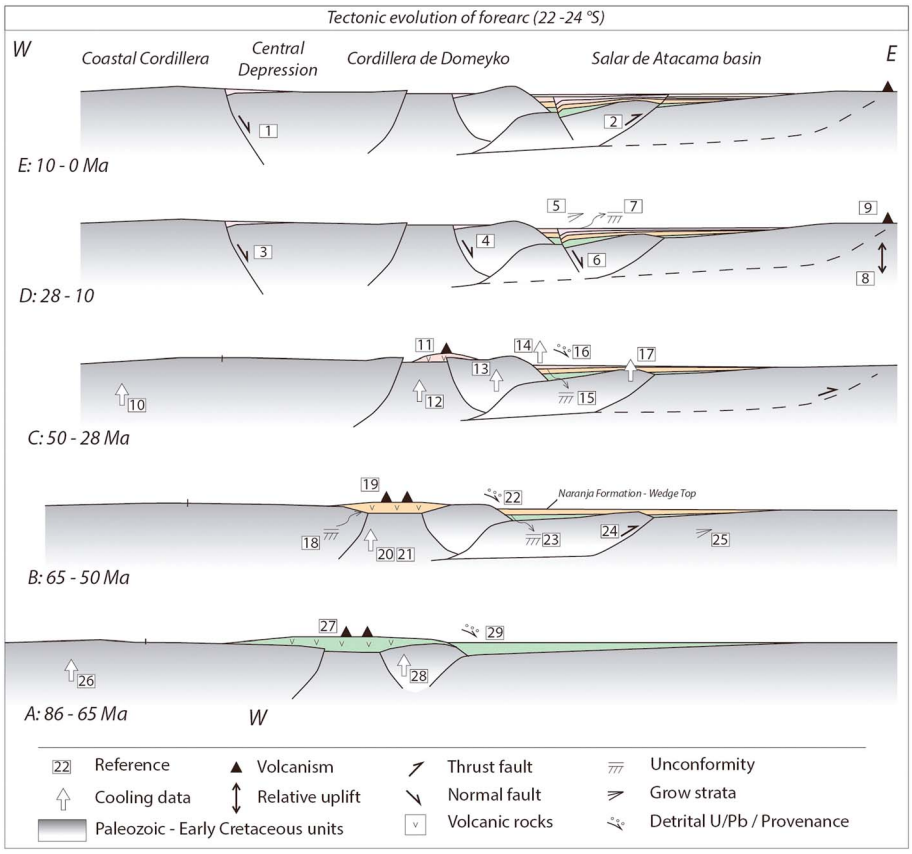

Figure 9. Schematic regional cross-sections through the western central Andes, showing proposed kinematic history as constrained by thermochronological data, unconformities, sedimentary provenance data, growth structures, and magmatism, based on this study and the references (denoted by numbered boxes) listed in Table S2 in supporting information. Different colors are used to distinguish different ages of volcano-sedimentary units.

5.3. Loma Amarilla Section

The distribution of detrital zircon U-Pb ages from the Naranja Formation (AT-NAJ, Figure 4) shows a Carboniferous, Jurassic and Upper Cretaceous age peaks (305, 171, and 73 Ma, Figure 4). We interpret the youngest peak (73.7 ± 1 Ma) as the maximum depositional age. Detrital zircon U-Pb data of the uppermost sample (1AT433DZ) from the Loma Amarilla Formation shows Permian, Triassic, Paleocene and Eocene peaks (296, 234, 57, and 42 Ma, Figure 4). The youngest age peak is 42.4 ± 0.8 Ma (Figure 4; see section 3.3), suggesting zircon provenance from the Eocene arc. We interpret the younger peak as the maximum depositional age for this part of the formation (see section 3.2). The U-Pb ages from the Naranja (AT-NAJ) and Loma Amarilla formations (1AT433DZ) show an increasing amount of Permian to Triassic zircon ages up-section relative to the amount of Cenozoic ages (Figure 4). The exposure of the Permian and Triassic source rocks together with the absence of the Jurassic source supports the unroofing signal proposed by Reiners et al. (2015). On the other hand, the youngest detrital AFT populations from the basal (64 ± 5.1 Ma, 1AT165FT) and middle (81.9 ± 8.8 Ma, 1AT433DZ) samples of the Loma Amarilla stratigraphic section indicate cooling of a source located in the CD. These cooling signals could be reflecting magmatic cooling or cooling associated with exhumation of the CD. The older cooling age signal in the middle part of the section compared to cooling age peak in the base of the section can also be explained by the unroofing of a volcanic sequence in the CD.

The AFT ages from the two granitic cobbles from the Loma Amarilla Formation (1AT1230FT and 1AT1450FT) indicate cooling at 56.7 ± 6.4 and 170.0 ± 18.4 Ma. These ages are not reset and therefore show the cooling age of the source terrane. Sample 1AT1230FT is Triassic in age (zircon U-Pb age of 234.7 ± 2.8 Ma). We interpret its AFT age to represent cooling driven by exhumation of at least ~2.5 km

of rocks from the CD (assuming 40 °C/km) between Paleocene time and the depositional age of the sample 1AT433DZ (42.4 ± 0.8 Ma). Reiners et al. (2015) reported an AFT age (32.9 ± 2.2 Ma, CL28, Figure 3) for the base of the Loma Amarilla Formation. The AHe ages reported in the same study for the same formation indicate cooling during the Paleocene and partial resetting during the Miocene (20–22 Ma). The AFT and the Paleocene AHe ages represent cooling of the source terrane (CD) prior to 32.9 ± 2.2 Ma, partial resetting due burial and later exhumation during the Miocene. This is likely related to the extensional episode during the Oligocene (e.g., Rubilar et al., 2017).

6. Discussion: Implications for the Behavior of the Orogenic Wedge

The review of previous and new cooling age data together with previous stratigraphic, provenance, geochronologic, and geochemical data helps to identify the location, timing, and magnitude of cooling and exhumation in the western sector of the central Andes since mid-Cretaceous time (Figures 8 and 9; section 5). Previous studies in the retroarc region of NW Argentina have documented rapid eastward propagation of the orogenic wedge at ~40 Ma and high elevations since ~38 Ma (Canavan et al., 2014; DeCelles et al., 2009, 2015; Quade et al., 2015). One result from our analysis is the correlation between times when the locus of exhumation controlled by deformation shifted eastward and regional unconformities developed in the CD and SA basin (Figures 8 and 9). The new data presented here from the western (hinterland) part of the orogenic system show three stages of exhumation at ~86–65, ~65–50, and ~50–28 Ma, which we discuss below in the context of Figures 8 and 9.

The Cretaceous cooling signal is consistent with exhumation and inversion of the Tarapaca extensional basin, which started at ~90 Ma (Amilibia et al., 2008). Mpodozis et al. (2005) interpreted the upper Cretaceous volcano-sedimentary deposits in the CD to be locally controlled by strike-slip deformation coeval with shortening in the retroarc region. Nonetheless, the evidence of late Cretaceous deformation in the hinterland is scarce. An unconformity observed at the base of the upper Cretaceous volcanic unit indicates that deformation and erosion occurred during the mid-Cretaceous in the Cordillera de Domeyko (e.g., Marinovic & García, 1999). Geochemical evidence from the magmatic arc indicates crustal thicknesses of ~35 km during the mid-Cretaceous (from Figure 2d in Profeta et al., 2015). Mid-Cretaceous exhumation has been reported in the Coastal Cordillera (which was in the forearc at that time; Maksaev & Zentilli, 1999; Juez-Larré et al., 2010; Reiners et al., 2015; Figures 3 and 9a), but the amount of erosion has not previously been estimated. Our results suggest ~2.5 km of erosion in the CD during the earliest stages in the orogeny. Presumably, exhumation related to this erosion was controlled by inversion of high-angle normal faults (in the Tarapaca basin), a process that would have been more efficient at exhuming rocks in the absence of substantial horizontal shortening. Given the apparent low amount of shortening (even considering the total amount of shortening in the CD), the normal crustal thickness (Profeta et al., 2015), the large amount of local exhumation in the CD, and the proximity between the arc and the foreland basin (Purilactis Formation in the SA basin), we speculate that flexural subsidence to accommodate ~3-km thick foreland basin deposits required either a large incipient thrust belt load or the contribution of additional loading from the arc itself (Figure 9a).

Between ~65 and ~50 Ma, the orogenic front was located either within the SA basin or east of the basin (Figure 9b). The migration of the orogenic front from somewhere in the CD to at least the middle part of the SA basin is supported by the presence of a depocenter east of the Cordon de Lila (Figure 2; based on interpretations by Arriagada et al., 2006) and by an angular unconformity in seismic line Z1G-010 (e.g., Arriagada et al., 2006; Jordan et al., 2007; Muñoz et al., 2002). This angular unconformity is also seen in the CD between ~22° and 26°S (e.g., Muñoz et al., 2002, Cornejo et al., 2003; Charrier et al., 2007; Figure 9b). Reverse faulting and folding have been documented along the CD and SA basin (e.g., Charrier et al., 2007; Cornejo et al., 2003). Considering the approximate position of the frontal thrust at that time (Figure 9b), the deformation in the CD was located in the hinterland and therefore corresponds to out-of-sequence deformation. As a consequence, the Naranja Formation in the SA basin was deposited in a wedge-top depozone within the proximal foreland basin system. Exhumation during this time is documented in the western part of the CD (Figures 3 and 8b; Maksaev & Zentilli, 1999; Reiners et al., 2015) and, according to our results, in the Loma Amarilla Formation (SA basin, Figures 7 and 8c). This is the first episode of cooling due to exhumation controlled by a reverse fault that is preserved in the CD (Figure 9b, references 20 and 21). The only available cooling age to the east is located in the easternmost CD and is an AFT

age for the Quimal intrusive (CHI-4, 64.9 ± 7.9 Ma, Andriessen & Reutter, 1994; Figure 6). As we argue in section 5.2, this age is, within error, contemporaneous to the crystallization age of the Quimal intrusive and could represent a magmatic cooling age. The sample (a cobble) from the Loma Amarilla Formation allows an estimation of ~2.5 km of exhumation from the CD between 56.7 ± 6.4 Ma and ~28 Ma (see section 5.3). Although the magnitude of exhumation between ~65 and 50 Ma remains unconstrained, the review of new and previous data allows us to identify and episode of cooling due to exhumation (not magmatic cooling) before ~50 Ma in the hinterland of the central Andean orogenic wedge (Figure 9b, reference 20, 21). Additionally, the crust may have thickened from ~35 to ~40 km (Profeta et al., 2015) during this time. Thus, the contractile deformation, timing and location of cooling due to exhumation, and the crustal thickening in the CD suggest a growing orogenic wedge. Retroarc foreland basin sedimentation took place in the Altiplano and Puna regions during this time (DeCelles & Horton, 2003; DeCelles et al., 2011; Horton, 2001). The presence of a foreland basin system in the Puna also suggests that the orogen had widened and propagated eastward by Paleocene to early Eocene time. By this time the orogenic wedge was growing by frontal accretion (manifested by the eastward propagation of the thrust belt) and by sporadic out-of-sequence deformation in the hinterland part of the wedge.

Deformation between ~50 and ~40 Ma has been traditionally interpreted as responsible for the construction of the central Andes between ~26° and 23°S (e.g., Bascuñan et al., 2015; Carrapa & DeCelles, 2015; Charrier et al., 2007; Mpodozis et al., 2005). Evidence for shortening during middle Eocene time is widely recognized in the central Andes (e.g., Coutand et al., 2001; DeCelles et al., 2015; Ege et al., 2007; Eichelberger et al., 2013; Horton, 2005; Horton et al., 2015; Oncken et al., 2006; Zhou et al., 2016). Geochemical and isotopic signatures suggest that the magmatic arc was forming in a progressively thicker crust (from ~40 km at 50 Ma to ~50 km at 40 Ma; Haschke et al., 2002, 2006; Profeta et al., 2015). Important changes in the size of the orogenic wedge took place between ~50 and 28 Ma: by 37 Ma, magmatism ceased in the CD (e.g., Coira et al., 1993; Haschke et al., 2002), and the thrust belt had propagated into the Puna and Eastern Cordillera (Figures 8 and 9c). In this context, the CD and SA basin transitioned from a location within the east facing retroarc orogenic wedge, to a hinterland position with locally derived sediments accumulating in intermontane basins. Eocene exhumation is recorded in both the hinterland region and the frontal orogenic wedge east of our study area (Carrapa & DeCelles, 2008). Cooling ages older than ~40 Ma generally are found in the forearc, whereas ages between ~40 and 28 Ma are found both in the forearc and retroarc (e.g., Carrapa & DeCelles, 2015). In the forearc, the axial part of the CD experienced 4–5 km of exhumation between 50 and 30 Ma, mostly between 40 and 30 Ma (Maksaev & Zentilli, 1999). The locus of exhumation was relocated to the eastern part of the CD (Figures 3 and 9c, references 13–17). New cooling ages from this study document the exhumation and erosion controlled by thrust faulting along the eastern edge of the CD starting at ~50 Ma (Figures 5 and 8). There, results from the Quimal Section (section 5.2) support the erosion of ~3.3 km of rocks between 50 and 28 Ma, ~1.6–3.3 km between ~50 and 40 Ma, and a maximum of ~1.7 km between 40 and 28 Ma. Finally, the Cordon de Lila (Figure 1) was cooled due to erosion and exhumation at ~38.6 ± 5.6 Ma (AFT age, Figure 2; Andriessen & Reutter, 1994) and at ~25 Ma (CL22, Figure 2; average age for three AHe single grain ages from Reiners et al., 2015) suggesting ~1.6 km of erosion between ~38.6 ± 5.6 and 25 Ma and ~1.6 km after ~25 Ma (assuming a geothermal gradient of 30 °C/km and a mean surface temperature of 20 °C). Additional exhumation due to thrusting along the eastern edge of the CD is recorded in the Barros Arana Syncline, where ~1.6 km of rocks had to be removed between ~32 Ma and the Miocene (See section 5.1). Exhumation data between ~50 and 40 Ma agree with the onset of the orogenic constructional phase proposed by Oncken et al. (2006) and correlate with an increase in convergence rates (Figure 8a) and the angular unconformity (directly to the east) between the Naranja and Loma Amarilla Formations. Although rapid exhumation and erosion due to internal shortening in the eastern part of the CD were occurring between ~50 and 28 Ma, the amount of shortening in the hinterland (CD and SA basin) was limited to <40 km (e.g., Amilibia et al., 2008). Haschke and Gunther (2003) estimated that shortening in the central part of the CD (~9 km) can explain up to 70% of the crustal thickness gained during this time and suggested that magmatic additions can account for the remaining 30%. If local shortening is unable to explain the crustal thickness, then other mechanisms should be considered. One of them is underplated material eroded from the forearc (e.g., Haxel et al., 2015; Von Huene & Scholl, 1991). Another option is basal accretion in the form of duplexes below the hinterland, which is able to balance the shortening in the frontal thrust belt (e.g., DeCelles et al., 2015). This period of increased exhumation and continuous crustal thickening preceded

the propagation of the orogenic front into the Puna and Eastern Cordillera and supports previous interpretations of a subcritical state and therefore unsteady growth of the central Andes during this time (Carrapa & DeCelles, 2015), either by frontal or by basal accretion.

Oligo-Miocene to recent exhumation is not recorded by low-temperature thermochronometers used in this study. Partially reset ages from the Loma Amarilla Formation support cooling due to the erosion of ~1.5–3 km of rocks (Reiners et al., 2015; Figure 7) during the Miocene, which is probably related to the Oligo-Miocene extensional episode (e.g., Rubilar et al., 2017). The lack of fully reset ages since the Oligocene supports limited erosion consistent with a dry climate and high regional elevation since mid-Miocene (Canavan et al., 2014; Quade et al., 2015). During this time, rapid exhumation, thrust faulting, and wedge-top deposits were mostly confined to the Eastern Cordillera (Carrapa & DeCelles, 2015 and references therein).

7. Conclusions

New apatite fission track and apatite (U-Th)/He data from upper Cretaceous to Eocene sedimentary rocks in the modern forearc region of the central Andes show Cretaceous to Oligocene cooling ages. We interpret the Late Cretaceous and younger ages to be the result of exhumation associated with major contractional deformation in the Cordillera de Domeyko in the early Andean retroarc thrust belt.

Cooling and exhumation could have started as early as~86 Ma and migrated eastward from the Coastal Cordillera and western part of the Cordillera de Domeyko to the eastern Cordillera de Domeyko and Salar de Atacama basin by ~65 Ma. Bedrock samples from the Cordillera de Domeyko thrust belt show cooling during the Paleocene and Eocene. Granite clasts from foreland basin conglomerates record cooling of the source terrane during the Late Cretaceous and Paleocene as well as a later Eocene exhumation of the thrust belt.

Based on the cooling ages and regional angular unconformities, three periods of exhumation are identified: ~86–65, ~65–50, and 50–28 Ma. We estimate that between ~2.5 and 3.3 km of erosion above major structures took place during these periods. Although exhumation during the Late Cretaceous is still poorly constrained, our results indicate that at least ~2.5 km of rocks were eroded away (at least locally) during this time. Exhumation after ~65 Ma is related to specific thrust fronts in the CD and corresponds to out-of-sequence deformation within the orogenic wedge.

Two angular unconformities in the Salar de Atacama basin at ~65 Ma and between ~50 and ~40 Ma are interpreted to be related to deformation and eastward propagation of the orogenic front. These deformation events progressively widened the orogen, relocating the orogenic front farther east of the magmatic arc. Results of this study provide support for models invoking shortening and orogenic growth of the Andean Cordillera since the Late Cretaceous, with an active continental arc, a retroarc thrust belt, and a foreland basin.

Acknowledgments
This research project has been funded by the GSA Research Grant and a grant from the U.S. National Science Foundation-Tectonics Program (EAR-071069). We thank Peter Reiners for the apatite (U-Th)/He data that were developed in the Arizona Radiogenic Helium Dating Laboratory (https://www.geo.arizona.edu/~reiners/arhdl/arhdl.htm) as part of the class Geochronology and Thermochronology at the University of Arizona. We wish to thank Andrea Goddard, James B. Chapman, and Silvia Cattò for support during lab work and interesting discussions. We also thank Valeria Zavala for her help in the field and R. N. Alonso for logistical support in Argentina. We thank all the reviewers, especially an anonymous reviewer whose comments helped to significantly improved the manuscript.

References

Allmendinger, R., Jordan, T., Kay, S., & Isacks, B. (1997). The evolution of the Altiplano-Puna Plateau of the central Andes. *Annual Review of Earth and Planetary Sciences*, *25*(1), 139–174. https://doi.org/10.1146/annurev.earth.25.1.139

Amilibia, A., Sabat, F., McClay, K. R., Muñoz, J. A., Roca, E., & Chong, G. (2008). The role of inherited tectono-sedimentary architecture in the development of the central Andean mountain belt: Insights from the Cordillera de Domeyko. *Journal of Structural Geology*, *30*(12), 1520–1539. https://doi.org/10.1016/j.jsg.2008.08.005

Andriessen, P. A., & Reutter, K. J. (1994). K–Ar and fission track mineral age determinations of igneous rocks related to multiple magmatic arc systems along the 23S latitude of Chile and Argentina. In *Tectonics of the Southern central Andes* (pp. 141–154). Berlin: Springer-Verlag. https://doi.org/10.1007/978-3-642-77353-2_10

Arriagada, C. (1999). Geología y Paleomagnetismo del Borde Oriental de la Cordillera de Domeyko entre los 2245 y 2330 latitud Sur. II Region, Chile. (MSc thesis, pp. 1–176). Chile: Universidad de Chile.

Arriagada, C., Cobbold, P. R., & Roperch, P. (2006). Salar de Atacama basin: A record of compressional tectonics in the central Andes since the mid-Cretaceous. *Tectonics*, *25*, TC1008. https://doi.org/10.1029/2004TC001770

Bascuñan, S., Arriagada, C., Le Roux, J., & Deckart, K. (2015). Unraveling the Peruvian Phase of the central Andes: Stratigraphy, sedimentology and geochronology of the Salar de Atacama Basin (22°30–23°S), northern Chile. *Basin Research*, *28*(3), 365–392. https://doi.org/10.1111/bre.12114

Basso, M., & Mpodozis, C. (2012). *Hoja Cerro Quimal*. Santiago, Chile: Serv. Nac. De Geol. y Miner.

Beck, S., & Zandt, G. (2002). The nature of orogenic crust in the central Andes. *Journal of Geophysical Research*, *107*(B10), 2230. https://doi.org/10.1029/2000JB000124

Campbell, I., Baillard, J., Pallin, J. M., Allen, C., & Fuentes, A. (2006). U-Pb zircon geochronology of granitic rocks from the Chuquicamata-El Abra porphyry copper belt of northern Chile: Excimer laser ablation ICP-MS analysis. *Economic Geology*, *101*(7), 1327–1344. https://doi.org/10.2113/gsecongeo.101.7.1327

Canavan, R., Carrapa, B., Clementz, M., Quade, J., DeCelles, P. G., & Schoenbohm, L. (2014). Early Cenozoic uplift of the Puna Plateau, central Andes, based on stable isotope paleoaltimetry of hydrated volcanic glass. *Geology*, *42*(5), 447–450. https://doi.org/10.1130/G35239.1

Carrapa, B., & DeCelles, P. G. (2008). Eocene exhumation and basin development in the Puna of northwestern Argentina. *Tectonics*, *27*, TC1015. https://doi.org/10.1029/2007TC002127

Carrapa, B., & DeCelles, P. G. (2015). Regional exhumation and kinematic history of the central Andes in response to cyclical orogenic processes. In P. G. DeCelles, M. N. Ducea, B. Carrapa, & P. A. Kapp (Eds.), *Geodynamics of a Cordilleran orogenic system: The central Andes of Argentina and Northern Chile*, *Geological Society of America Memoir* (Vol. 212 (2015) 1212(11), pp. 201–213). https://doi.org/10.1130/2015.1212(11)

Carrapa, B., DeCelles, P. G., Reiners, P. W., Gehrels, G. E., & Sudo, M. (2009). Apatite triple dating and white mica 40Ar/39Ar thermochronology of syntectonic detritus in the Central Andes: A multiphase tectonothermal history. *Geology*, *37*(5), 407–410. https://doi.org/10.1130/G25698A.1

Charrier, R., Pinto, L., & Rodríguez, M. P. (2007). Tectonostratigraphic evolution of the Andean orogen in Chile. In T. Moreno & W. Gibbons (Eds.), *The Geology of Chile* (pp. 21–114). London: Geol. Soc.

Charrier, R., & Reutter, K. J. (1994). The Purilactis group of northern Chile: Boundary between arc and backarc from Late Cretaceous to Eocene. In K. J. Reutter, E. Scheuber, & P. Wigger (Eds.), *Tectonics of the southern central Andes: Structure and evolution of an active continental margin* (pp. 189–202). New York: Springer. https://doi.org/10.1007/978-3-642-77353-2_13

Coira, B., Kay, S. M., & Viramonte, J. (1993). Upper Cenozoic magmatic evolution of the Argentine Puna—A model for changing subduction geometry. *International Geology Review*, *35*(8), 677–720. https://doi.org/10.1080/00206819309465552

Cornejo, P., Matthews, S., & Perez, C. (2003). The "K-T" compressive deformation event in northern Chile (24°–27°S). In *Proceedings 10th Congreso Geológico Chileno*, In CD (Thematic session 1, 11 p.). Concepción, Chile: Universidad de Concepción.

Coutand, I., Cobbold, P. R., Urreiztieta, M., Gautier, P., Chauvin, A., Gapais, D., et al. (2001). Style and history of Andean deformation, Puna plateau, northwestern Argentina. *Tectonics*, *20*(2), 210–234. https://doi.org/10.1029/2000TC900031

DeCelles, P. G., Carrapa, B., Horton, B. K., & Gehrels, G. E. (2011). Cenozoic foreland basin system in the central Andes of northwestern Argentina: Implications for Andean geodynamics and modes of deformation. *Tectonics*, *30*, TC6013. https://doi.org/10.1029/2011TC002948

DeCelles, P. G., Ducea, M. N., Kapp, P., & Zandt, G. (2009). Cyclicity in Cordilleran orogenic systems. *Nature Geoscience*, *2*, 251–257. https://doi:10.1038/ngeo469

DeCelles, P. G., & Horton, B. K. (2003). Early to middle tertiary foreland basin development and the history of Andean crustal shortening in Bolivia. *Geological Society of America Bulletin*, *115*(1), 58–77. https://doi.org/10.1130/0016-7606(2003)115<0058:ETMTFB>2.0.CO;2

DeCelles, P. G., Zandt, G., Beck, S. L., Currie, C. A., Ducea, M. N., Kapp, P., et al. (2015). Cyclical orogenic processes in the Cenozoic central Andes. *Geological Society of America Memoirs*, *212*, MWR212–MWR222. https://doi.org/10.1130/2015.1212(22

Dickinson, W. R., & Gehrels, G. E. (2009). Use of U–Pb ages of detrital zircons to infer maximum depositional ages of strata: A test against a Colorado Plateau Mesozoic database. *Earth and Planetary Science Letters*, *288*(1–2), 115–125. https://doi.org/10.1016/j.epsl.2009.09.013

Donelick, R. A., O'Sullivan, P. B., & Ketcham, R. A. (2005). Apatite fission-track analysis. *Reviews in Mineralogy and Geochemistry*, *58*(1), 49–94. https://doi.org/10.2138/rmg.2005.58.3

Ege, H., Sobel, E. R., Scheuber, E., & Jacobshagen, V. (2007). Exhumation history of the southern Altiplano plateau (southern Bolivia) constrained by apatite fission track thermochronology. *Tectonics*, *26*, TC1004. https://doi.org/10.1029/2005TC001869

Ehlers, T. A., & Farley, K. A. (2003). Apatite (U-Th)/He thermochronometry; methods and applications to problems in tectonic and surface processes. *Earth and Planetary Science Letters*, *206*(1-2), 1–14. https://doi.org/10.1016/S0012-821X(02)01069-5.

Eichelberger, N., McQuarrie, N., Ehlers, T. A., Enkelmann, E., Barnes, J. B., & Lease, R. O. (2013). New constraints on the chronology, magnitude, and distribution of deformation within the central Andean orocline. *Tectonics*, *32*, 1432–1453. https://doi.org/10.1002/tect.20073

Eichelberger, N., McQuarrie, N., Ryan, J., Karimi, B., Beck, S., & Zandt, G. (2015). Evolution of crustal thickening in the central Andes, Bolivia. *Earth and Planetary Science Letters*, *426*, 191–203. https://doi.org/10.1016/j.epsl.2015.06.035

Farley, K. A. (2000). Helium diffusion from apatite: General behavior as illustrated by Durango fluorapatite. *Journal of Geophysical Research*, *105*(B2), 2903–2914. https://doi.org/10.1029/1999JB900348

Flint, S., Turner, P., Jolley, E. J., & Hartley, A. J. (1993). Extensional tectonics in convergent margin basins: An example from the Salar de Atacama, Chilean Andes. *Geological Society of America Bulletin*, *105*(5), 603–617. https://doi.org/10.1130/0016-7606(1993)105<0603:ETICMB>2.3.CO;2

Flowers, R. M. (2009). Exploiting radiation damage control on apatite (U–Th)/He dates in cratonic regions. *Earth and Planetary Science Letters*, *277*(1-2), 148–155. https://doi.org/10.1016/j.epsl.2008.10.005

Galbraith, R. F. (2005). *Statistics for fission track analysis*. New York: Chapman and Hall/CRC. https://doi.org/10.1201/9781420034929

Garcia, A. F. (1967). Geología del Norte Grande de Chile. Symposium sobre el Geosinclinal Andino. In *Sociedad Geológica de Chile, Publicación* (138 pp.). Santiago, Chile.

Gautheron, C., Tassan-Got, L., Ketcham, R. A., & Dobson, K. J. (2012). Accounting for long alpha-particle stopping distances in (U–Th–Sm)/He geochronology: 3D modeling of diffusion, zoning, implantation, and abrasion. *Geochimica et Cosmochimica Acta*, *96*, 44–56. https://doi.org/10.1016/j.gca.2012.08.016

Gehrels, G. E., Valencia, V. A., & Ruiz, J. (2008). Enhanced precision, accuracy, efficiency, and spatial resolution of U-Pb ages by laser ablation–multicollector–inductively coupled plasma–mass spectrometry. *Geochemistry, Geophysics, Geosystems*, *9*, Q03017. https://doi.org/10.1029/2007GC001805

Giese, P. (1994). Geothermal structure of the Central Andean crust—Implications for heat transport and rheology. In *Tectonics of the southern Central Andes* (pp. 69–76). Berlin, Heidelberg: Springer. https://doi.org/10.1007/978-3-642-77353-2_4

Gleadow, A. J. W., Duddy, I. R., Green, P. F., & Lovering, J. F. (1986). Confined fission track lengths in apatite: A diagnostic tool for thermal history analysis. *Contributions to Mineralogy and Petrology*, *94*(4), 405–415. https://doi.org/10.1007/BF00376334

González, G., Cembrano, J., Carrizo, D., Macci, A., & Schneider, H. (2003). The link between forearc tectonics and Pliocene–Quaternary deformation of the Coastal Cordillera, northern Chile. *Journal of South American Earth Sciences*, *16*(5), 321–342. https://doi.org/10.1016/S0895-9811(03)00100-7

Götze, H. J., & Krause, S. (2002). The central Andean gravity high, a relic of an old subduction complex? *Journal of South American Earth Sciences*, *14*(8), 799–811. https://doi.org/10.1016/S0895-9811(01)00077-3

Green, P. F. (1981). A new look at statistics in fission-track dating. *Nuclear Tracks*, *5*(1–2), 77–86. https://doi.org/10.1016/0191-278X(81)90029-9

Hartley, A. J., & Evenstar, L. (2010). Cenozoic stratigraphic development in the north Chilean forearc: Implications for basin development and uplift history of the Central Andean margin. *Tectonophysics*, *495*(1–2), 67–77. https://doi.org/10.1016/j.tecto.2009.05.013

Hartley, A. J., May, G., Chong, G., Turner, P., Kape, S. J., & Jolley, E. J. (2000). Development of a continental forearc: A Cenozoic example from the Central Andes, northern Chile. *Geology*, *28*(4), 331–334. https://doi.org/10.1130/0091-7613(2000)28<331:DOACFA>2.0.CO;2

Haschke, M., & Gunther, A. (2003). Balancing crustal thickening in arcs by tectonic vs. magmatic means. *Geology*, *31*(11), 933–936. https://doi.org/10.1130/G19945.1

Haschke, M., Siebel, W., Günther, A., & Scheuber, E. (2002). Repeated crustal thickening and recycling during the Andean orogeny in north Chile (21–26 S). *Journal of Geophysical Research*, *107*(B1), 2019. https://doi.org/10.1029/2001JB000328

Haxel, G. B., Jacobson, C. E., & Wittke, J. H. (2015). Mantle peridotite in newly discovered far-inland subduction complex, southwest Arizona: Initial report. *International Geology Review*, *57*(5–8), 871–892. https://doi.org/10.1080/00206814.2014.928916

Henríquez, S. M., Becerra, J., & Arriagada, C. (2014). Geología del área San Pedro de Atacama, Región de Antofagasta. Servicio Nacional de Geología y Minería. Carta Geológica de Chile, Serie Geología Básica, 1.

Horton, B. K. (2005). Revised deformation history of the central Andes: Inferences from Cenozoic foredeep and intermontane basins of the Eastern Cordillera, Bolivia. *Tectonics*, *24*, TC3011. https://doi.org/10.1029/2003TC001619

Horton, B. K., Hampton, B. A., & Waanders, G. L. (2001). Paleogene synorogenic sedimentation in the Altiplano plateau and implications for initial mountain building in the central Andes. *Geological Society of America Bulletin*, *113*(11), 1387–1400. https://doi.org/10.1130/0016-7606(2001)113<1387:PSSITA>2.0.CO;2

Horton, B. K., Perez, N. D., Fitch, J. D., & Saylor, J. E. (2015). Punctuated shortening and subsidence in the Altiplano plateau of southern Peru: Implications for early Andean mountain building. *Lithosphere*, *7*(2), 117–137. https://doi.org/10.1130/L397.1

Hurford, A. J., & Green, P. F. (1982). A users' guide to fission track dating calibration. *Earth and Planetary Science Letters*, *59*(2), 343–354. https://doi.org/10.1016/0012-821X(82)90136-4

Hurford, A. J., & Green, P. F. (1983). The zeta age calibration of fission-track dating. *Chemical Geology*, *41*, 285–317. https://doi.org/10.1016/S0009-2541(83)80026-6

Isacks, B. L. (1988). Uplift of the central Andean plateau and bending of the Bolivian orocline. *Journal of Geophysical Research*, *93*(B4), 3211–3231. https://doi.org/10.1029/JB093iB04p03211

Jordan, T. E., Mpodozis, C., Munoz, N., Blanco, N., Pananont, P., & Gardeweg, M. (2007). Cenozoic subsurface stratigraphy and structure of the Salar de Atacama Basin, northern Chile. *Journal of South American Earth Sciences*, *23*(2–3), 122–146. https://doi.org/10.1016/j.jsames.2006.09.024

Jordan, T. E., Nester, P. L., Blanco, N., Hoke, G. D., Dávila, F., & Tomlinson, A. J. (2010). Uplift of the Altiplano-Puna Plateau: A view from the west. *Tectonics*, *29*, TC5007. https://doi.org/10.1029/2010TC002661

Juez-Larré, J., Kukowski, N., Dunai, T. J., Hartley, A. J., & Andriessen, P. A. (2010). Thermal and exhumation history of the Coastal Cordillera arc of northern Chile revealed by thermochronological dating. *Tectonophysics*, *495*(1–2), 48–66. https://doi.org/10.1016/j.tecto.2010.06.018

Ketcham, R. A., Donelick, R. A., & Carlson, W. D. (1999). Variability of apatite fission-track annealing kinetics: III. Extrapolation to geological time scales. *American Mineralogist*, *84*(9), 1235–1255. https://doi.org/10.2138/am-1999-0903

Macellari, C. E., Su, M. J., & Townsend, F. (1991). Structure and seismic stratigraphy of the Atacama Basin, Northern Chile. In *Proc. VI Congr. Geol. Chileno* (Vol. 1, pp. 133–137). Chile: Universidad de Chile.

Maksaev, V., & Zentilli, M. (1999). Fission track thermochronology of the Domeyko Cordillera, northern Chile: Implications for Andean tectonics and porphyry copper metallogenesis. *Exploration and Mining Geology*, *8*(1/2), 65–90.

Marinovic, N., & García, M. (1999). Hoja Pampa Unión, Región de Antofagasta. Servicio nacional de geología y minería.

Marinovich, N., & Lahsen, A. (1984). Hoja Calama, Región de Antofagasta. Carta Geológica de Chile. Servicio Nacional de Geología y Minería, Chile, 140.

May, G., Hartley, A. J., Stuart, F. M., & Chong, G. (1999). Tectonic signatures in arid continental basins: An example from the Upper Miocene–Pleistocene, Calama Basin, Andean forearc, northern Chile. *Palaeogeography, Palaeoclimatology, Palaeoecology*, *151*(1–3), 55–77. https://doi.org/10.1016/S0031-0182(99)00016-4

May, G., Hartley, H., Chong, G., Stuart, F., Turner, P., & Kape, S. (2005). Eocene to Pleistocene lithostratigraphy, chronostratigraphy and tectono-sedimentary evolution of the Calama Basin, northern Chile. *Revista Geológica de Chile*, *32*(1), 33–58.

McQuarrie, N. (2002). Initial plate geometry, shortening variations, and evolution of the Bolivian orocline. *Geology*, *30*(10), 867–870. https://doi.org/10.1130/0091-7613(2002)030<0867:IPGSVA>2.0.CO;2

McQuarrie, N., & Ehlers, T. (2017). Techniques for understanding fold-and-thrust belt kinematics and thermal evolution. In R. D. Law, J. R. Thigpen, A. J. Merschat, & H. H. Stowell (Eds.), *Linkages and feedbacks in orogenic systems*, *Geological Society of America Memoir 213* (pp. 25–54). https://doi.org/10.1130/2017.1213(02)

Mpodozis, C., Arriagada, C., Basso, M., Roperch, P., Cobbold, P., & Reich, M. (2005). Late Mesozoic to Paleogene stratigraphy of the Salar de Atacama Basin, Antofagasta, northern Chile: Implications for the tectonic evolution of the Central Andes. *Tectonophysics*, *399*(1–4), 125–154. https://doi.org/10.1016/j.tecto.2004.12.019

Muñoz, N., Charrier, R., & Jordan, T. (2002). Interactions between basement and cover during the evolution of the Salar de Atacama Basin, northern Chile. *Revista Geologica de Chile*, *29*(1), 55–80. https://doi.org/10.4067/S0716-02082002000100004

Muñoz, N., Charrier, R., & Reutter, J. K. (1997). Evolución de la Cuenca del Salar de Atacama: Inversión tectónica y relleno de una cuenca de antepaís de retroarco, paper presented at VIII Congreso Geológico Chileno. University Católica del Norte, Antofagasta, Chile.

Naranjo, J. A., Ramirez, C. F., & Pankoff, R. (1994). Morphostratigraphic evolution of the northwestern margin of the Salar de Atacama basin (23 S–68 W). *Andean Geology*, *21*(1), 91–103.

Okada, A. (1971). On the neotectonics of the Atacama fault zone region. Preliminary notes on late Cenozoic faulting and geomorphic development of the Coast Range of northern Chile. *Bulletin of the Department of Geography, University of Tokyo*, *3*, 47–65.

Oncken, O., Hindle, D., Kley, J., Elger, K., Victor, P., & Schemmann, K. (2006). Deformation of the central Andean upper plate system—Facts, fiction, and constraints for plateau models. In *The Andes* (pp. 3–27). Berlin Heidelberg: Springer. https://doi.org/10.1007/978-3-540-48684-8_1

Pananont, P., Mpodozis, C., Blanco, N., Jordan, T. E., & Brown, L. D. (2004). Cenozoic evolution of the northwestern Salar de Atacama Basin, northern Chile. *Tectonics*, *23*, TC6007. https://doi.org/10.1029/2003TC001595

Pardo-Casas, F., & Molnar, P. (1987). Relative motion of the Nazca (Farallon) and South American plates since Late Cretaceous time. *Tectonics*, *6*(3), 233–248. https://doi.org/10.1029/TC006i003p00233

Profeta, L., Ducea, M. N., Chapman, J. B., Paterson, S. R., Henriquez, S., Kirsch, M., et al. (2015). Quantifying crustal thickness over time in magmatic arcs. *Scientific Reports*, *5*(1), 17786. https://doi.org/10.1038/srep17786

Quade, J., Dettinger, M. P., Carrapa, B., DeCelles, P., Murray, K. E., Huntington, K. W., et al. (2015). The growth of the central Andes, 22 S–26 S. *Geological Society of America Memoirs*, *212*, 277–308. https://doi.org/10.1130/2015.1212(15)

Reiners, P. W., & Brandon, M. T. (2006). Using thermochronology to understand orogenic erosion. *Annual Review of Earth and Planetary Sciences*, *34*(1), 419–466. https://doi.org/10.1146/annurev.earth.34.031405.125202

Reiners, P. W., & Nicolescu, S. (2006). Measurement of parent nuclides for (U-Th)/He chronometry by solution sector ICP-MS, ARHDL Report 1. Retrieved from http://www.geo.arizona.edu/~reiners/arhdl/arhdl.htm

Reiners, P. W., Thomson, S. N., Vernon, A., Willett, S. D., Zattin, M., Einhorn, J., et al. (2015). Low-temperature thermochronologic trends across the central Andes, 21 S–28 S. *Geological Society of America Memoirs*, *212*, 215–249. https://doi.org/10.1130/2015.1212(12)

Reutter, K. J., Charrier, R., Götze, H. J., Schurr, B., Wigger, P., Scheuber, E., et al. (2006). The Salar de Atacama Basin: a subsiding block within the western edge of the Altiplano-Puna Plateau. In *The Andes* (pp. 303–325). Berlin, Heidelberg: Springer. https://doi.org/10.1007/978-3-540-48684-8_14

Rothstein, D. A., & Manning, C. E. (2003). *Geothermal gradients in continental magmatic arcs: Constraints from the eastern Peninsular Ranges batholith* (pp. 337–354). Baja California, México: Special Papers-Geological Society of America.

Rubilar, J., Martínez, F., Arriagada, C., Becerra, J., & Bascuñán, S. (2017). Structure of the Cordillera de la Sal: A key tectonic element for the Oligocene-Neogene evolution of the Salar de Atacama basin, Central Andes, northern Chile. *Journal of South American Earth Sciences*, *87*, 200–210. https://doi.org/10.1016/j.jsames.2017.11.013

Sáez, A., Cabrera, L., Jensen, A., & Chong, G. (1999). Late Neogene lacustrine record and palaeogeography in the Quillagua–Llamara basin, central Andean fore-arc (northern Chile). *Palaeogeography, Palaeoclimatology, Palaeoecology*, *151*(1–3), 5–37. https://doi.org/10.1016/S0031-0182(99)00013-9

Servicio Nacional de Geología y Minería (2003). Mapa Geológico de Chile. 1 Mapa escala 1:1,000,000. Santiago, Chile.

Shuster, D. L., Flowers, R. M., & Farley, K. A. (2006). The influence of natural radiation damage on helium diffusion kinetics in apatite. *Earth and Planetary Science Letters*, *249*(3–4), 148–161. https://doi.org/10.1016/j.epsl.2006.07.028

Soler, P., & Bonhomme, M. G. (1990). Relation of magmatic activity to plate dynamics in central Peru from Late Cretaceous to present. *Geological Society of America Special Papers*, *241*, 173–192. https://doi.org/10.1130/SPE241-p173

Vermeesch, P. (2009). RadialPlotter: A Java application for fission track, luminescence and other radial plots. *Radiation Measurements*, *44*(4), 409–410. https://doi.org/10.1016/j.radmeas.2009.05.003

Von Huene, R., & Scholl, D. W. (1991). Observations at convergent margins concerning sediment subduction, subduction erosion, and the growth of continental crust. *Reviews of Geophysics*, *29*(3), 279–316. https://doi.org/10.1029/91RG00969

Wilkes, E., & Görler, K. (1994). Sedimentary and structural evolution of the Salar de Atacama depression. In *Tectonics of the southern central Andes* (pp. 171–188). Berlin, Heidelberg: Springer. https://doi.org/10.1007/978-3-642-77353-2_12

Zhou, R., Schoenbohm, L. M., Sobel, E. R., Carrapa, B., & Davis, D. W. (2016). Sedimentary record of regional deformation and dynamics of the thick-skinned southern Puna Plateau, central Andes (26–27°S). *EPSL*, *433*, 317–325. https://doi.org/10.1016/j.epsl.2015.11.012